# Evaluation of constitutive models for shear-banding wormlike micellar solutions in simple and complex flows

Journal of Non-Newtonian Fluid Mechanics 307 (2022) 104855

Contents lists available at ScienceDirect

Journal of Non-Newtonian Fluid Mechanics

journal homepage: www.elsevier.com/locate/jnnfm

# Evaluation of constitutive models for shear-banding wormlike micellar solutions in simple and complex flows

Stylianos Varchanis [a,*], Simon J. Haward [a], Cameron C. Hopkins [a], John Tsamopoulos [b], Amy Q. Shen [a,*]

[a] Micro/Bio/Nanofluidics Unit, Okinawa Institute of Science and Technology, 1919-1 Tancha, Onna, 904-0495, Okinawa, Japan
[b] Laboratory of Fluid Mechanics & Rheology, Department of Chemical Engineering, University of Patras, Caratheodory 1, Patras, 26504, Achaia, Greece

ARTICLE INFO

*Keywords:*
Wormlike micellar solution
Shear-banding
Johnson–Segalman
Giesekus
Thixotropic
Viscoelastic
VCM
Elastic instability
Stress diffusion
Poiseuille flow
Cross-slot
Flow past a cylinder
Bi-stability

ABSTRACT

Wormlike micellar solutions possess complex rheology: when exposed to a flow field, the wormlike micelles may orientate, stretch, and break into smaller micelles. Entangled wormlike micellar solutions exhibit shear banding characteristics: macroscopic bands with different local viscosities are organized and stacked along the velocity gradient direction, leading to a non-monotonic flow curve in simple shear. We present a systematic analysis of four commonly used constitutive models that can predict a non-monotonic flow curve and potentially describe the rheology of entangled wormlike micellar solutions with shear-banding characteristics: the Johnson–Segalman, the Giesekus, the thixotropic viscoelastic, and the Vasquez–Cook–McKinley (VCM) models. All four constitutive models contain a stress diffusion term, to account for a smooth transition between the shear bands and ensure a uniqueness of the numerical solution. Initially, the models are fitted to shear and extensional experimental data of a shear-banding wormlike micellar solution. Subsequently, they are employed to solve three non-homogeneous flows: the Poiseuille flow in a planar channel, the flow in a cross-slot geometry, and the flow past a cylinder in a straight channel. Each of these flows exposes the wormlike micellar solution to different flow kinematics (shear, extensional, and mixed), revealing different aspects of its rheological response. The predictive capability of each model is evaluated by directly comparing the numerical results to previously published experimental data obtained from microfluidic devices with corresponding flow configurations. While all the models can describe qualitatively the characteristic features observed experimentally in the benchmark flows, such as plug-like velocity profiles and elastic instabilities, none of them yields a quantitative agreement. Based on the overall performance of the models and also accounting for their differing numerical complexity, we conclude that the Giesekus model is at present the most suitable constitutive equation for simulating shear banding wormlike micellar solutions in flows that exhibit both shear and extensional deformations. However, the quantitative mismatch between model predictions and experiments with wormlike micellar solutions demand that improved constitutive models be developed in future works.

## 1. Introduction

Surfactants are amphiphilic molecules that consist of a hydrophobic tail and a bulky hydrophilic headgroup, which can be neutrally, positively, or negatively charged [1]. In aqueous solution, when the surfactant concentration is increased above a critical micellar concentration (CMC), surfactant monomers will spontaneously self-assemble into large aggregates known as micelles in order to shield the hydrophobic tails from water [2,3]. There is a wide variety of possible morphologies that micelles can adopt, depending on factors such as the temperature, pH, concentration, salinity, surfactant packing parameter, and flow conditions [4]. For certain surfactants, as the concentration is increased above the CMC, spherical micelles form and further grow into elongated rod-like surfactant aggregates with increasing surfactant concentrations [1]. Wormlike micelles (WLMs) are formed as the micellar length grows above the persistence length, thus rendering the micelles semi-flexible and in many ways similar to semi-flexible polymer molecules [1]. Wormlike micelles can be described as long, semi-flexible cylindrical aggregates that can entangle, and similarly to polymer chains, attribute viscoelasticity to the solution [5–7]. In contrast to polymers, WLMs exist in a dynamic equilibrium, undergoing reversible scission and recombination; this provides additional stress

* Corresponding authors.
*E-mail addresses:* varchanis@hotmail.com (S. Varchanis), amy.shen@oist.jp (A.Q. Shen).

https://doi.org/10.1016/j.jnnfm.2022.104855
Received 15 November 2021; Received in revised form 4 June 2022; Accepted 20 June 2022
Available online 23 June 2022

relaxation mechanisms, which can cause flow-induced morphological changes (e.g., gel formation), or lead to recovery of their bulk viscoelastic properties after micellar degradation that may occur in strong flows [8,9]. The fact that WLMs exhibit such highly tunable properties is mirrored in their extensive industrial use as drag-reduction agents, in oil recovery processes, and also as rheology modifiers in cosmetics, personal care, and food products [10–13]. Given the plethora of their applications, a comprehensive understanding of the rheological behaviour of these fluids under different flow kinematics is of crucial importance.

From a rheological perspective, experimental observations [10,14,15] have shown that the linear viscoelastic response of entangled WLMs at low and medium frequencies can be described by a single-mode Maxwellian relaxation spectrum. The addition of a Newtonian solvent or a second Maxwellian mode can describe the high frequency upturn usually observed in the loss modulus. In some cases, the shape of the loss modulus curve at very high frequencies suggests shear thinning effects, making the two mode-approximation necessary. Nevertheless, the fact that WLMs can be adequately fitted with a single-mode constitutive equation, plus a viscous contribution, makes them ideal model viscoelastic fluids [16]. Despite their simplicity in the linear regime, their rheological fingerprint becomes more complicated in the regime of nonlinear deformations. The flow curve (shear stress *versus* shear rate in simple shear) of a WLM solution under certain conditions of temperature, concentration, and salinity [17], exhibits a so-called "stress plateau" (see Fig. 1). At low shear rates, the stress grows proportionally to the shear rate, but after a critical value of the shear rate ($\dot{\gamma} > \dot{\gamma}_1$), a plateau in the stress is observed, often spanning a wide range of shear rates. As discussed by Vasquez et al. [18], sheared WLM solutions in a circular Couette geometry (Taylor–Couette, TC) have revealed the formation of two primary "shear bands". A high shear rate band near the inner or moving wall consisting of broken, short, and aligned micelles. A low shear rate band near the outer or fixed wall consisting of unbroken entangled micelles [19–21]. With increasing imposed shear rate, more micelles break and the high shear rate band increases in width, at the cost of a decreasing width of the low shear rate band. At very high shear rates ($\dot{\gamma} > \dot{\gamma}_2$), the flow curve rises again because all the micelles are broken and the solution behaves like a Newtonian fluid. This non-monotonicity in the flow curve constitutes a hysteresis and is the most characteristic feature of shear-banding fluids. Finally, experiments with WLMs under uniaxial and planar extension [22–25] suggest that WLMs exhibit extension hardening when the WLM micelles start to stretch, followed by extension thinning at higher extension rates, due to micelle breakage.

In the limit of vanishing inertia, the combination of extreme shear-thinning with extension-hardening effects triggers a wide variety of elastic instabilities in various flows. These unexpected flow configurations are caused by the interaction of the stretching, breaking, and reforming micelles with the macroscopic flow. Some of the most representative examples are the oscillations in the velocity of a sphere sedimenting in a WLM solution [26–28], the asymmetric flow profiles in cross-slot geometries [24,25,29,30], the onset of secondary vortex flows [31,32] and waves [33] in TC flow, the asymmetric flow profiles past a single or an array of cylinders in a channel [34–39], and the synchronization phenomena in flows where WLMs interact with flexible structures [40–42].

Based on the aforementioned rheological characteristics of WLMs, one can envision that the constitutive modelling of such fluids is a very challenging task. Many sophisticated models, which are based on microstructural theories, have been proposed over the last decades. The "living polymers" model by Cates [5] is considered to be a starting point for the majority of studies that focus on the derivation of constitutive equations for WLMs. This concept, along with several other relevant improvements, have led to the development of constitutive models that, presumably, can describe the flow of WLMs in both linear and nonlinear regimes [43–47]. Recent studies [48,49] have introduced

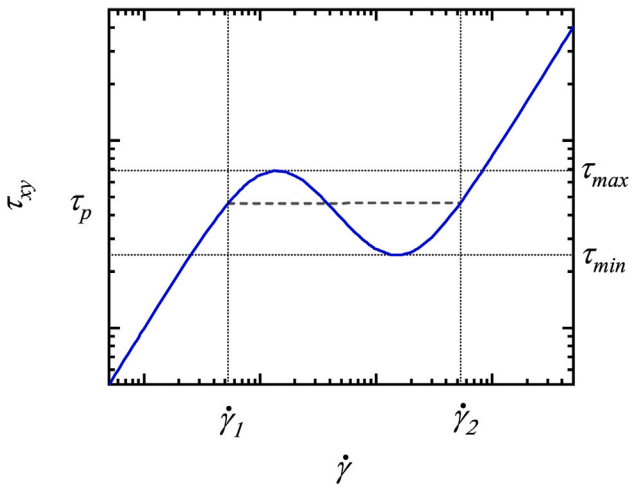


**Fig. 1.** Qualitative representation of a non-monotonic flow curve (shear stress *versus* shear rate in simple shear). The horizontal dashed line shows a possible stress for shear banded flow, with material on either the low or high shear rate branches. The negative slope portion of the curve represents mechanically unstable homogeneous flows.

population balances in constitutive equations for WLM solutions; these new models provide more accurate descriptions of nonlinear stress relaxation dynamics. However, the problem with all these models is that they can only be used in very simple flows; in general, they are too complicated to be solved when coupled with the momentum and mass conservation in computational fluid dynamics (CFD) simulations. According to Bird et al. [50], an ideal model should predict the realistic properties of the relevant fluid, feature the minimum possible number of material parameters, and be computationally manageable in complex flows. In almost any case of a non-Newtonian fluid, the satisfaction of all these conditions seems to be impossible. Nevertheless, in favour of gaining some insight into the response of WLMs in complex flows, several assumptions must be made in the choice of constitutive equations in CFD simulations. Thus, we can identify two possible strategies for the simulation of shear-banding WLMs: (1) adopting a phenomenological constitutive equation that can predict a non-monotonic flow curve, or (2) making the necessary assumptions to derive a constitutive equation that is based on microstructural theories, but is simple enough to be solved in a complex flow. Some characteristic examples from the first group are the Johnson–Segalman (JS) model [51] and the Giesekus (GS) model [52], while two characteristic examples from the second group are the Vasquez–Cook–McKinley (VCM) model [18] and the simplified living Rolie-Poly model [53].

In this paper, we aim to answer which is the most suitable existing constitutive model for CFD simulations with shear-banding WLM solutions. We choose to examine the JS, GS, and VCM models because they are the most frequently encountered models in CFD simulations of WLM solutions [54–60]. Despite their popularity, they have never been directly compared to experimental data in 2-dimensional flows, where both shear and extensional deformations take place; instead, their predictive capabilities versus real fluids have only been assessed in planar and cylindrical Couette flows [61–64]. Finally, we include a phenomenological, thixotropic viscoelastic (TVE) constitutive equation [65] as a cheaper alternative to the VCM model. The paper is organized as follows: in Section 2, we present and discuss the various constitutive models. In Section 3, we fit the models to shear and extensional rheometric data of an entangled WLM solution and estimate the relevant material parameters of each model. In Section 4, we describe the flow geometries, state the governing equations and boundary conditions of the flow, and discuss the numerical method used to solve them. In Sections Section 5, 6, and 7, we solve the models in three benchmark flows: (1) the purely shear flow in a planar channel, (2)

the extension dominated flow in the cross-slot extensional rheometer, and (3) the flow past a cylinder in a channel with low blockage ratio. The predictions of the models are directly compared to experimental data. Finally, conclusions are drawn in Section 8.

## 2. Constitutive models

### 2.1. The Johnson–Segalman (JS) model

Based on the continuum theory of viscoelasticity [51], the Johnson–Segalman (JS) model was introduced as a generalization of the constitutive equation for viscoelastic fluids obtained from the network theory by Lodge [66]. The fundamental difference between the JS and the Upper Convected Maxwell constitutive equations is the definition of the objective derivative that attributes frame invariance to the model. The JS constitutive equation expressed in terms of the conformation tensor $\mathbf{C}$ is given as:

$$\frac{1+\zeta}{2}\overset{\triangledown}{\mathbf{C}}+\frac{1-\zeta}{2}\overset{\triangle}{\mathbf{C}}+\frac{\mathbf{C}-\mathbf{I}}{\lambda}=D\nabla^2\mathbf{C}, \tag{1}$$

where $\lambda$ is the relaxation time of the fluid, $\zeta$ is a nonlinear parameter that governs the definition of the objective derivative, and $D$ is the stress diffusion coefficient. Additionally, the symbols $\triangledown$ and $\triangle$ over the conformation tensor denote the upper and lower convected derivatives, respectively, and $\mathbf{I}$ denotes the unit tensor. The extra stress tensor is given as the sum of the contributions from the macromolecules (or, in this case micelles) and the solvent:

$$\boldsymbol{\tau}=\frac{G}{\zeta}(\mathbf{C}-\mathbf{I})+\eta_s\dot{\boldsymbol{\gamma}}, \tag{2}$$

where $G$ is the elastic modulus, $\eta_s$ is the viscosity of the solvent, and $\dot{\boldsymbol{\gamma}} = \nabla\mathbf{u}+\nabla\mathbf{u}^T$ is the deformation rate tensor, with $\mathbf{u}$ denoting the velocity of the fluid. The nonlinear parameter $\zeta$ governs the degree of shear thinning and the ratio of the first to second normal stress difference in simple shear. For $-1 < \zeta < 1$ and $0 < \eta_s < 1/9$ the model always predicts a non-monotonic flow curve, and thus, shear-banding. In terms of physical interpretation, the downturn in the flow curve (Fig. 1) occurs due to non-affine deformation of the junctions of the network. The presence of the stress diffusion term [67] in the constitutive equation is necessary because it provides a smooth transition between the shear bands and a uniqueness of the numerical solution when the flow is shear banded [68]. The JS model is meant to describe polymer solutions and melts, but because of its ability to predict a non-monotonic flow curve, it has also been employed to model WLM solutions. Its main advantage is its simplicity; the JS model is quasi-linear, meaning that for a given velocity field, the resulting equation is linear. Its major drawbacks are that it predicts unphysical results in step strain and infinite stresses in purely extensional flows beyond a critical value of the extension rate [4].

### 2.2. The Giesekus (GS) model

Giesekus [52] proposed the GS model based on the dumbbell kinetic theory by including anisotropic hydrodynamic drag and Brownian motion to account for polymer–polymer interactions in concentrated polymer solutions or polymer melts. The GS constitutive equation is given as:

$$\overset{\triangledown}{\mathbf{C}}+\frac{\mathbf{C}-\mathbf{I}}{\lambda}+\frac{\alpha(\mathbf{C}-\mathbf{I})^2}{\lambda}=D\nabla^2\mathbf{C}. \tag{3}$$

In this nonlinear model, $\alpha$ is the mobility parameter, which controls the degree of shear thinning, the ratio of the second to first normal stress difference, and the maximum value of extensional viscosity. Eq. (2) with $\zeta = 1$ is used to obtain the extra stress tensor. For $0.5 < \alpha < 1$ and relatively small values of the solvent to total viscosity ratio $\beta = \eta_s/(G\lambda+\eta_s)$, the model can predict a non-monotonic flow curve (Fig. 1). From a physical point of view, the downturn in the flow curve is attributed to an effective reduction of the drag coefficient on each chain due to the modification of the flow field by the flow of the surrounding chains. The GS model is a well-known, widely used, and studied model that can predict inhomogeneous flows of a wide class of non-Newtonian fluids [69–71]. Its ability to predict a non-monotonic flow curve along with its numerical stability have made it a popular choice for CFD simulations of WLM solutions, and a point of reference for the present study. While the GS model can describe accurately almost any flow curve, it usually fails to describe the extensional rheology of the same sample using the same set of parameters and a single-mode approximation.

### 2.3. The thixotropic viscoelastic (TVE) model

The TVE model is a simplified version of the nonlinear constitutive equation recently proposed by Varchanis et al. [65]. The aforementioned constitutive model, referred to as the TEVP model, is a very general phenomenological constitutive equation that can describe a wide class of thixotropic elasto-visco-plastic materials [65,72]. In the present work, the plastic effects in the model are neglected, resulting to a thixotropic viscoelastic (TVE) model, and the set of the simplified equations are given as:

$$\overset{\triangledown}{\mathbf{C}}+\frac{\mathbf{C}-\mathbf{I}}{\lambda_{ef}}=D\nabla^2\mathbf{C}, \tag{4}$$

$$\frac{Ds}{Dt}=k_1(1-s)-k_2(\dot{\boldsymbol{\gamma}}:\mathbf{C})s+D\nabla^2 s. \tag{5}$$

Here $s$ is a non-dimensional structure parameter, which is introduced to indicate the instantaneous degree of "structure" of the micelles in the solution, and $D/Dt$ denotes the material derivative. It varies in a predetermined range ($0 < s \leq 1$) with limits corresponding to the two extreme cases regarding the rheological response of the solution; when $s = 1$, the micelles are assumed to behave as in equilibrium, forming long cylindrical structures, when $s \to 0$, the micelles are assumed to be fully broken into very short structures. The structure of the micelles directly affects the relaxation time of the solution; this is taken into account by introducing an effective relaxation time that is proportional to the relaxation time of the solution and the structure parameter: $\lambda_{ef} = \lambda s^m$, where $m$ is a positive adjustable parameter. The positive constants $k_1$ and $k_2$ govern the magnitude of the rate of reforming and breakage of the micelles. Eq. (2) with $\zeta = 1$ is used to obtain the extra stress tensor. In fact, this model belongs to the family of modified Bautista–Manero (MBM) constitutive equations [73–77] (see Appendix A). Although the TVE and the MBM models are derived from slightly different phenomenological arguments, setting $m = 1$ and considering that $s \equiv G\lambda/\phi$ ($\phi$ is the so-called "fluidity" parameter used in the MBM models, see Appendix A) will yield an identical set of equations: an Oldroyd-B fluid with a thixotropic relaxation time and polymeric viscosity [78]. Their basic difference is how shear-banding is induced in each model. In the TVE model, the non-monotonicity in the flow curve is driven by an extreme reduction of the relaxation time of the fluid due to breakage of the micelles (exponential decay of $s$). Note that the TVE model can predict a non-monotonic flow curve only if $m > 1$. On the other hand, a term proportional to the magnitude of the deformation rate is added at the destruction term of MBM model [74] (see Appendix A) to make the curve non-monotonic. As we will demonstrate in the next section, a major advantage of the TVE model is that it can fit both the shear and extensional rheometric data with the same set of material parameters. However, this gain is counterbalanced by the increased number of material parameters when compared to the previous two models, and the extra computational cost for solving Eq. (5).

### 2.4. The Vasquez-Cook-McKinley (VCM) model

The VCM model is inspired by Cates' "living polymer" model [5,8,43] and is derived based on principles of the kinetic theory [18]. In this model, the WLMs are represented by species A and species B. The micelles that are longer than the statistical average in the equilibrium state of rest are represented by species A. On the other hand, species B represent the shorter micelles. A micelle that belongs to species A is allowed to break in half and form two micelles that belong to species B. Additionally, two micelles that belong to species B can recombine and form one micelle that belongs to species A, satisfying the detailed balance. The VCM model is given as:

$$\mu\lambda\frac{Dn_A}{Dt} = \frac{c_B n_B^2}{2} - c_A n_A + 2D_A\lambda_A\nabla^2 n_A, \tag{6}$$

$$\mu\lambda\frac{Dn_B}{Dt} = 2c_A n_A - c_B n_B^2 + 2D_B\lambda_B\nabla^2 n_B, \tag{7}$$

$$\mu\lambda\overset{\triangledown}{\mathbf{A}} + \mathbf{A} - n_A\mathbf{I} + c_A\mathbf{A} - c_B n_B\mathbf{B} = D_A\lambda_A\nabla^2\mathbf{A}, \tag{8}$$

$$\epsilon\mu\lambda\overset{\triangledown}{\mathbf{B}} + \mathbf{B} - \frac{n_B}{2}\mathbf{I} + 2\epsilon\left(c_B n_B\mathbf{B} - c_A\mathbf{A}\right) = \epsilon D_B\lambda_B\nabla^2\mathbf{B}. \tag{9}$$

Here $n_A$ and $n_B$ denote the dimensionless number densities for species A and B, respectively. The configuration tensors for species A and B are denoted as $\mathbf{A}$ and $\mathbf{B}$. The interested reader may refer to Vasquez et al. [18] for a detailed definition of the variables $(n_A, n_B, \mathbf{A}, \mathbf{B})$ and the derivation of the VCM model. The relaxation time for species A and species B are given as $\lambda_A$ and $\lambda_B$, and the stress diffusion coefficients as $D_A$ and $D_B$. The effective relaxation time of the fluid is given as $\lambda$, as in the previous models. The dimensionless breakage rate of the long micelles is defined as $c_A = c_{A,0} + \frac{\mu\lambda\xi}{3}(\dot{\boldsymbol{\gamma}} : \frac{\mathbf{A}}{n_A})$ and the dimensionless reforming rate is defined as $c_B = c_{B,0}$, where $c_{A,0}$ and $c_{B,0}$ are their values at equilibrium. We also define the ratios $\mu = \lambda_A/\lambda = 1 + c_{A,0}$ and $\epsilon = \lambda_B/\lambda_A$. Finally, the extra stress tensor is retrieved by the relation:

$$\boldsymbol{\tau} = G(\mathbf{A} - n_A\mathbf{I} + 2\mathbf{B} - n_B\mathbf{I}). \tag{10}$$

In this model, shear-banding arises because of the alignment of the WLMs and their flow-induced breakage [61]. Although there have been some refinements to the VCM model [79,80], we will stick to its initial version, because it is the most popular choice in CFD simulations [54,55,57]. The main advantage of the VCM model is that it is expected to describe, at least qualitatively, the physics related to the flow of WLMs because it is derived from microstructural arguments. Its disadvantage is the high computational cost related to its solution; one must solve two tensorial and two scalar equations to obtain the extra stress tensor.

## 3. Fluid rheology

The various constitutive models described above are used to mimic a shear-banding wormlike micellar solution composed of 100 mM CPyCl and 60 mM NaSal dissolved in deionized water. This is a well studied surfactant/counterion system known to form entangled wormlike micelles [14,81].

The fluid has been characterized in prior literature in small amplitude oscillatory shear (SAOS), simple shear, and steady planar extension [24,25,37,38,41]. The storage modulus, $G'(\omega)$, the loss modulus, $G''(\omega)$, the steady shear stress, $\tau_{xy}(\dot{\gamma})$, and the steady first planar extensional viscosity, $\eta_e(\dot{\epsilon})$, are shown in Figs. 2–4. Note that $\omega$ is the angular frequency in SAOS, $\dot{\gamma}$ is the shear rate in simple shear, and $\dot{\epsilon}$ is the extension rate at the stagnation point in planar extension.

The estimation of the material parameters of the constitutive models is performed as follows. Initially, the relaxation spectrum of each model is estimated from the SAOS experiment. The remaining nonlinear parameters of each model are next fitted simultaneously to the rheometric flows (simple shear and steady planar extension). A description of the nonlinear regression process is given by Varchanis et al. [69]. The material functions used for the determination of material parameters are the storage and loss moduli, $G'$ and $G''$, the steady shear stress, $\tau_{xy}(\dot{\gamma})$, and the steady first planar extensional viscosity, $\eta_e(\dot{\epsilon})$. The adjustable parameters are the relaxation spectrum, $G$, $\lambda$, $\eta_s$ for JS, GS, and TVE models and $G$, $\lambda$, $\sqrt{2c_{A,0}/c_{B,0}}$, $\lambda_B$ for the VCM model, and each model's nonlinear parameters. The stress diffusion coefficient cannot be estimated from the homogeneous rheometric experiments, and its determination will be discussed at the end of this section. The values of the material parameters that yielded the best curve fit are given in Table 1.

**Table 1**
Material parameters of the models.

| Model | JS | GS | TVE | VCM |
|---|---|---|---|---|
| $G$ [Pa] | 33 | 33 | 33 | 33 |
| $\lambda$ [s] | 3 | 3 | 3 | 3 |
| $\eta_s$ [Pa s] | 0.01 | 0.01 | 0.01 | – |
| $\lambda_B$ | – | – | – | 0.00032 |
| $\zeta$ | 0.97 | – | – | – |
| $\alpha$ | – | 0.83 | – | – |
| $m$ | – | – | 2.16 | – |
| $k_1$ [$s^{-1}$] | – | – | 0.0058 | – |
| $k_2$ | – | – | 0.0017 | – |
| $c_{A,0}$ | – | – | – | 1.78 |
| $c_{B,0}$ | – | – | – | 3.92 |
| $\xi$ | – | – | – | 0.35 |
| $D$ [$m^2$ $s^{-1}$] | $\mathcal{O}(10^{-11})$ | $\mathcal{O}(10^{-11})$ | $\mathcal{O}(10^{-11})$ | $\mathcal{O}(10^{-11})$ |

### 3.1. Small amplitude oscillatory shear (SAOS)

In the linear regime, the JS, GS, and TVE models reduce to a single-mode Maxwell model plus a viscous contribution in parallel. Thus, the corresponding expressions of the storage and loss moduli are given as:

$$G' = G\frac{(\lambda\omega)^2}{1+(\lambda\omega)^2}, \tag{11}$$

$$G'' = G\frac{\lambda\omega}{1+(\lambda\omega)^2} + \eta_s\omega. \tag{12}$$

The VCM model reduces to a double-mode Maxwell model, and the corresponding expressions are [18]:

$$G' = G\frac{(\lambda\omega)^2}{1+(\lambda\omega)^2} + G\sqrt{\frac{2c_{A,0}}{c_{B,0}}}\frac{(\lambda_B\omega)^2}{1+(\lambda_B\omega)^2}, \tag{13}$$

$$G'' = G\frac{\lambda\omega}{1+(\lambda\omega)^2} + G\sqrt{\frac{2c_{A,0}}{c_{B,0}}}\frac{\lambda_B\omega}{1+(\lambda_B\omega)^2}. \tag{14}$$

In order to compare the models on equal basis, $G$ and $\lambda$ are common among all models. Note that $\eta_s$ (JS, GS, TVE) and the product $G\lambda_B\sqrt{2c_{A,0}/c_{B,0}}$ (VCM) are restricted by the asymptotic value of the shear viscosity, $\eta_{sh} = \tau_{xy}/\dot{\gamma}$, at the limit of very high shear rates in simple shear. Thus, based on the high shear rate plateau (see Fig. 3(b)), $\eta_s$ and $G\lambda_B\sqrt{2c_{A,0}/c_{B,0}}$ cannot attain values more than 0.01 Pa s. Fig. 2 presents the fittings of the storage and loss moduli to the experimental data from [25]. Note that the value of $\lambda_B$ is very small (see Table 1(b)) and the curves produced by JS, GS, and TVE models (Eqs. (11) and (12)) and those by the VCM model (Eqs. (13)–(14)) collapse. As we observe, all the models can capture the relaxation spectrum of this WLM solution well, except for the upturn of $G''$. This happens because the values of $\eta_s$ and $G\lambda_B\sqrt{2c_{A,0}/c_{B,0}}$ are restricted by the high shear rate plateau in the flow curve (see Fig. 3). Nevertheless, the frequency at which the upturn takes place is well captured by the models.

### 3.2. Simple shear

The velocity field of a WLM solution under simple shear flow is assumed to obey the well-known kinematics, $\mathbf{u} = (\dot{\gamma}y, 0, 0)$, while the stress field is assumed to be homogeneous. These assumptions probably

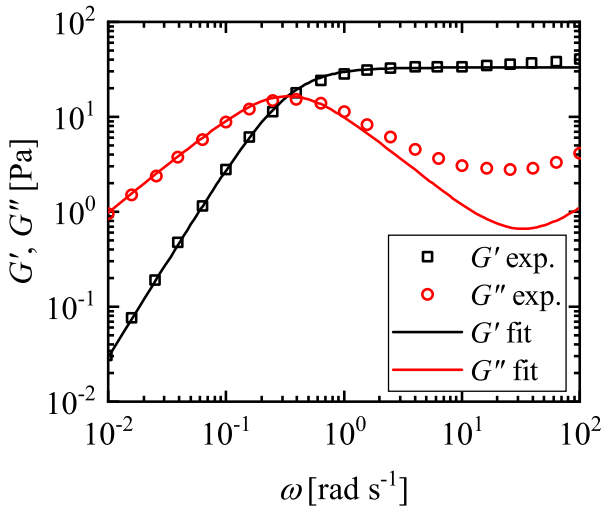


**Fig. 2.** Fittings of the storage and loss moduli (lines) to the experimental data from [25] (symbols). Note that the value of $\lambda_B$ used in the VCM model is very small and the curves produced by JS, GS, and TVE models (Eqs. (11)–(12)) and those by the VCM model (Eqs. (13)–(14)) collapse.

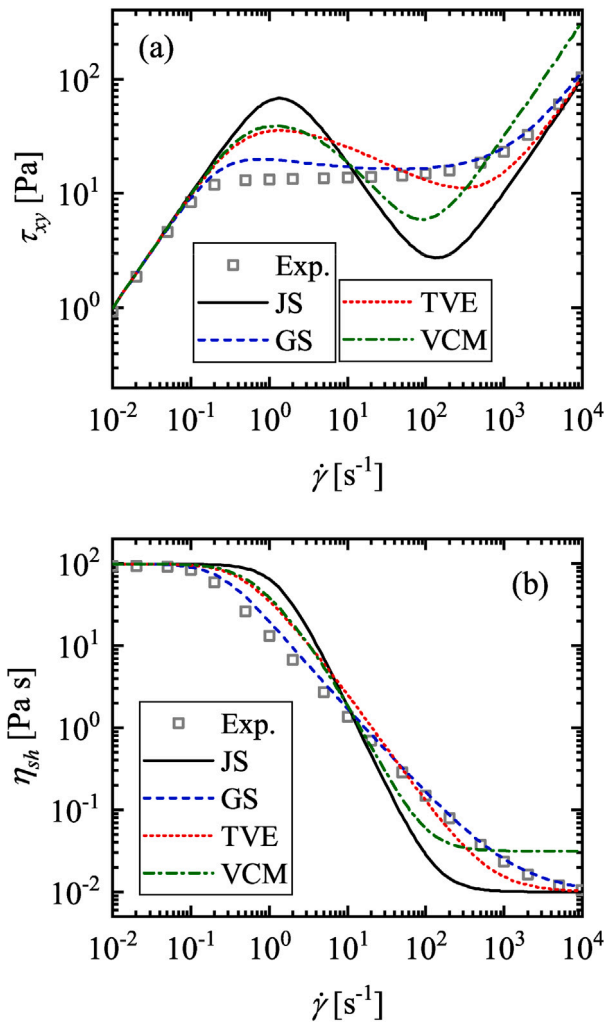


**Fig. 3.** (a) Shear stress *versus* shear rate. (b) Shear viscosity *versus* shear rate. Comparison between experimental results [25] (symbols) and the predictions from the four constitutive models (lines).

do not hold in the experiment because the flow is expected to be shear-banded at the plateau region, and thus, non-homogeneous. However, the homogeneous stress assumption will not affect the fit of the models; previous studies [62–64,82] have shown that even when spatial distributions of the stresses are considered, the average value of the shear stress in the gap always lies in between the limits defined by the hysteresis in the homogeneous flow curve.

Fig. 3 presents the predictions of the models regarding the steady shear stress and the steady shear viscosity ($\eta_{sh} = \tau_{xy}/\dot{\gamma}$) *versus* the shear rate (assuming flow homogeneity), superimposed to the experimental data. First of all, we observe that the fluid is strongly shear-banding; the stress plateau spans almost four decades in the logarithmic distribution of the shear rate. The shape of the hysteresis in simple shear can provide valuable information regarding inhomogeneous flows. The larger the difference between $\dot{\gamma}_2$ and $\dot{\gamma}_1$ ($\Delta\dot{\gamma} = \dot{\gamma}_2 - \dot{\gamma}_1$, see Fig. 1), the sharper the boundary layer on the velocity profile between two shear bands in inhomogeneous flows will be. This happens because for a given interface thickness, the shear rate difference will be larger, leading to a higher velocity gradient, and a sharper boundary layer. Moreover, a large difference between the maximum and minimum stress values along the hysteresis ($\Delta\tau = \tau_{max} - \tau_{min}$, see Fig. 1) promotes metastable states, for which a metastable, unbanded flow can be maintained indefinitely [83]. In Fig. 3, the JS model (black solid curve) predicts huge $\Delta\dot{\gamma}$ and $\Delta\tau$ along the hysteresis. Thus, we expect that the JS model will predict a very sharp boundary layer in the velocity distributions and promoted metastability, leading to abrupt transitions between unbanded and banded flow configurations. Proceeding to the GS model (blue dashed curve), we observe that $\Delta\dot{\gamma}$ is smaller, while $\Delta\tau$ is barely visible. This means that the velocity boundary layers will be milder and the transitions from unbanded to banded flows smoother. The TVE and VCM models (red dotted and green dashed curves, respectively) give similar predictions, which exhibit smaller $\Delta\dot{\gamma}$ and $\Delta\tau$ than the JS model and larger than the GS model. Therefore, their inhomogeneous response is expected to lie in between the JS and GS models, assuming that the interface thickness is the same in all models.

### 3.3. Steady planar extension

Extensional flows are a very crucial part of the calibration process of the constitutive models to experimental data. The fitting of the models to extensional data provides the information on how the fluid behaves under tension and complements the information obtained from the fitting to the shear data. In the case of ideal steady planar extension, the velocity field is given as $\mathbf{u} = (\dot{\varepsilon}x, -\dot{\varepsilon}y, 0)$, while the stress field is homogeneous.

Fig. 4 illustrates the comparison between the experimental data for the steady first planar extensional viscosity and the predictions of each model. It is well known [18,23] that WLM solutions exhibit extension hardening at low extension rates ($\lambda\dot{\varepsilon} \approx 0.5$), followed by extension thinning at higher extension rates. This is clearly illustrated in the experimental data by Haward et al. [25]. The extensional viscosity predicted by the JS model becomes infinite as $\lambda\dot{\varepsilon} = 0.5$ is approached, and the model completely fails to describe the experimental data. Although the addition of the stress diffusion term will remove the singularity in non-homogeneous flows [67], the JS model will still overpredict the extensional response of the solution. In contrast to the JS model, the GS model underpredicts the extensional viscosity for the whole range of $\dot{\varepsilon}$. Proceeding to the TVE model, we observe that it can predict the correct shape of the curve, but still underestimates the extensional viscosity. Finally, the VCM model yields the best agreement with the experimental data in steady planar extension.

Before proceeding to the next section, it is very important to discuss the value that we chose for the stress diffusion coefficient, $D$. As we mentioned above, one cannot fit the value of $D$ to rheometric data because the stress Laplacian term vanishes in homogeneous flows. Experimental studies regarding the value of the stress

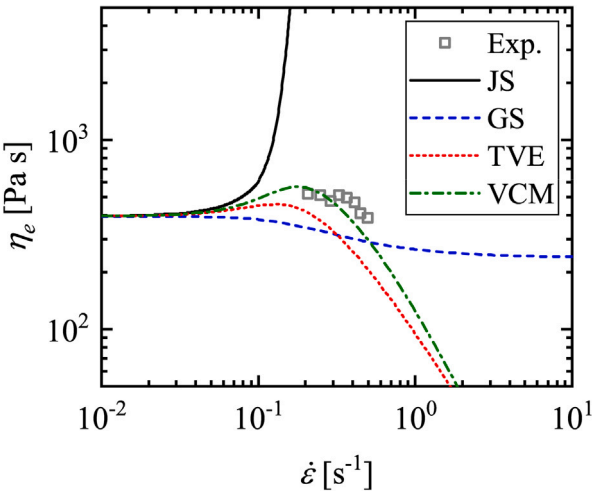


**Fig. 4.** First planar extensional viscosity *versus* extension rate. Comparison between experimental results [25] (symbols) and the predictions from the four constitutive models (lines).

diffusion coefficient in WLM solutions report values in the range $10^{-13} < D < 10^{-8}$ m$^2$ s$^{-1}$ [84–87]. Some studies have also reported that $D$ can depend on the shear rate [87] and on the lengthscale [85] of the flow. However, in terms of CFD simulations, the main role of $D$ is to provide a smooth transition between the shear bands, removing the discontinuity from the shear rate profiles, and to provide a unique numerical solution. The thickness of the interface between the shear bands is proportional to the quantity $\sqrt{D\lambda}$ [68,88]. Thus, the value of $D$ should be large enough to guarantee a unique numerical solution, but also small enough so that it does not affect the rheological properties of the fluid, producing nonphysical diffusive effects in the constitutive equation. A simple and efficient rule for choosing $D$ in numerical simulations is given by Fielding and coworkers [89,90], $\sqrt{D\lambda} \sim 10^{-2}H$, where $H$ is the width of the flow channel. Based on the channels that we are going to study, $H \sim \mathcal{O}(10^{-4}$ m), and the relaxation time of the fluid ($\lambda = 3$ s), we find that $D \sim \mathcal{O}(10^{-11}$ m$^2$ $s^{-1})$; note that this value of $D$ is consistent with the experimental measurements in similar WLM solutions [84].

## 4. Modelling of non-homogeneous flows

### 4.1. Flow geometries

In the numerical simulations, we consider the 2D creeping flow of a WLM solution in three geometries: (1) a planar straight channel, (2) a cross-slot that is formed by the intersection of two planar channels, and (3) a planar channel that contains a circular cylinder located midway between the walls [see Fig. 5]. The fluid is incompressible with constant density $\rho$, solvent viscosity $\eta_s$, polymeric viscosity $\eta_p = G\lambda$, and zero shear viscosity $\eta_0 = \eta_p + \eta_s$ at zero shear rate. The width of the channel is denoted $H$ and the radius of the cylinder $R$. The length of the channel in the Poiseuille flow is equal to $30H$ and the length of the inflow and outflow channels in the cross-slot is equal to $10H$. In the case of the cylinder, the width of the channel is $H = 20R$ and the total length of the channel is equal to $250R$. The average velocity of the solution in each channel is denoted as $U$. In the case of the Poiseuille flow and the cross-slot we scale all lengths with the width of the channel ($L \equiv H$), while in the case of the cylinder we scale all lengths with the radius of the cylinder ($L \equiv R$). All velocities are scaled with the average flow velocity $U$, and all times with the characteristic flow time $L/U$. In addition, both the pressure and stress components are scaled with the viscous scale, $\eta_0 U/L$. The dimensionless groups that arise are the Weissenberg number, $Wi = \lambda U/L$, the Newtonian solvent-to-total viscosity ratio $\beta = \eta_s/\eta_0$, and the dimensionless diffusivity $Di = D\lambda/H^2$. Based on the selection of the stress diffusion coefficient, $D$ (see Section 3), $Di = 10^{-3}$ in all the flows that we present with the GS, TVE and VCM models. In the simulations with the JS model we used $Di = 3 \times 10^{-3}$, because we could not obtain numerically stable solutions in the shear-banded regime with smaller values of $Di$. Any gravitational phenomena are neglected, due to the small lengthscale of the flow cells.

### 4.2. Governing equations

The non-Newtonian flow is described by the incompressible and isothermal Cauchy equations coupled with a constitutive equation, which accounts for the contribution of the non-Newtonian stresses. Neglecting inertia, the forms of the continuity, momentum, and constitutive equations are expressed, respectively, as:

$$\nabla \cdot \mathbf{u} = 0, \tag{15}$$

$$\nabla \cdot \left(-P\mathbf{I} + \boldsymbol{\tau} + \eta_s \dot{\boldsymbol{\gamma}}\right) = \mathbf{0}, \tag{16}$$

$$\mathbf{g}(\boldsymbol{\tau}, \nabla\mathbf{u}) = \mathbf{0}, \tag{17}$$

where $P$ is thermodynamic pressure and the operator $\mathbf{g}$ corresponds to any of the constitutive models presented in Section 2.

The no-slip and no-penetration boundary conditions ($\mathbf{u} = \mathbf{0}$) are imposed on the channel walls and the cylinder surface. At the inflow boundaries, we impose fully developed velocity and stress fields for the JS, GS and TVE models. Regarding the VCM model, we impose a plug velocity profile ($\mathbf{u} = [U, 0]$) and zero stresses ($n_A = 1$, $n_B = \sqrt{2c_{A,0}/c_{B,0}}$, $\mathbf{A} = \mathbf{I}$, $\mathbf{B} = 0.5\sqrt{2c_{A,0}/c_{B,0}}\mathbf{I}$) along the inflow boundaries; we employ this technique to avoid the specification of $n_A$ and $n_B$ via conservation integrals at the inflow boundaries. In order to eliminate any additional numerical error that could arise due to the truncation of the domain, the open boundary condition (OBC) [91] has been applied along the outflow boundaries. According to the OBC, the fluid velocities and stresses are not imposed at the outflow boundary but are calculated from the weak form of the equations for both velocity unknowns (extrapolated from the bulk). Finally, additional boundary conditions are needed regarding the stress field, the structure variable, and the dimensionless number densities at the walls of the geometries; this happens because of the presence of the stress Laplacian term in the constitutive equation. Although the correct type of boundary conditions for the stress field is still under discussion [92], we will adopt the simplest possible choice, viz, zero gradient for the stresses, structure variable and dimensionless number densities ($\mathbf{n} \cdot \nabla \boldsymbol{\tau} = \mathbf{0}$, $\mathbf{n} \cdot \nabla s = 0$, $\mathbf{n} \cdot \nabla n_{A,B} = 0$), where $\mathbf{n}$ is the unit normal vector on the fluid–solid interfaces.

### 4.3. Numerical method

The Petrov–Galerkin stabilized Finite Element Method for viscoelastic flows (PEGAFEM-V), proposed by Varchanis et al. [93–95], is used to solve the governing equations. The aforementioned finite element (FE) method makes use of linear interpolants for all variables. The variational formulation along with a detailed explanation of the FE method is given by Varchanis et al. [95]. Note that we did not use any transformation to enforce the positive definiteness of the conformation tensor (e.g. log-conformation reformulation) because the stress Laplacian term facilitates the simulations at high values of $Wi$. In all simulations, we use a structured mesh, composed by triangular elements. A mesh convergence study is presented in Appendix B.

For a given set of flow parameters ($Wi$, $\beta$, and the remaining material parameters of each model), we first perform transient simulations. If a steady state is obtained by the transient simulation, then it is

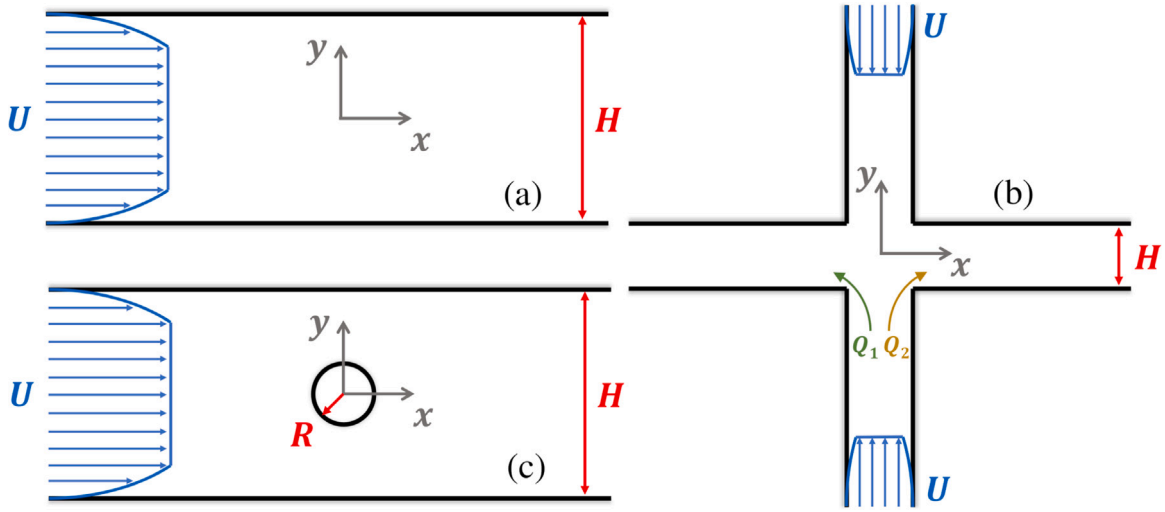


**Fig. 5.** Schematic of the flow geometries. (a) Planar channel flow. (b) Cross-slot flow. (c) Flow past a cylinder in a straight channel.

used as the initial guess for direct steady state simulations at the same values of the flow parameters. In the direct steady state simulations, the time derivatives in the governing equations (Eqs. (16)–(17)) are neglected, and the $Wi$ number is gradually altered; this process is called parameter continuation. In order to trace the families of the steady solution branches in the parametric space, we employ the pseudo-arc-length continuation algorithm [96], as implemented in the FEM framework by Varchanis et al. [97]. This handling enables efficient tracking of pitchfork and saddle–node bifurcations in the parametric space. Furthermore, using the bifurcation theory and the fact that the parameter continuation starts from a steady state obtained by transient simulations, we can determine whether a solution branch is stable or unstable.

## 5. Shear flow

After evaluating in detail the predictions of each model in simple rheometric flows, the next step is to test them in more complex problems of practical importance. In this section, we consider the steady channel flow of the model WLM solution under the imposition of a constant flow rate per unit depth, $Q = UH$ (Fig. 5(a)). The width of the channel is $H = 400\ \mu m$. This flow resembles a simple shear flow since only shear deformations are experienced by the fluid, but in this case, the velocity field is not provided externally; instead, it is calculated by solving the mass and momentum balances along with the constitutive model (Eqs. (15) and (17)). Another crucial difference between this channel flow and simple shear flow is that the shear rate in the former is not constant but exhibits a spatial variation. Thus, shear-banding can arise, enabling us to evaluate the predictive capability of each model by directly comparing their predictions with the experimental data by Haward et al. [37].

Fig. 6 presents the predictions of each model for the velocity profiles, superimposed to the experimental ones (square symbols). The experimental flow profiles were obtained by particle image velocimetry (PIV) [37]. Two values of $Wi$ are examined, both of which lead to shear-banding and plug-like velocity profiles. Regarding the experiment, the velocity profile features a finite curvature for the low flow rate ($Wi = 2.1$), with the maximum value of the dimensionless velocity being equal to $u_{x,max}/U \approx 1.1$. Almost perfect plug flow is observed at higher flow rates ($Wi = 10.4$), with the dimensionless velocity being equal to 1 across the channel. The predictions by the JS, GS, and VCM models match nicely with the experimental profiles velocity profiles for both values of $Wi$. All three of them predict plug-like flow and similar high shear rate bands near the wall. As expected by the shape of the

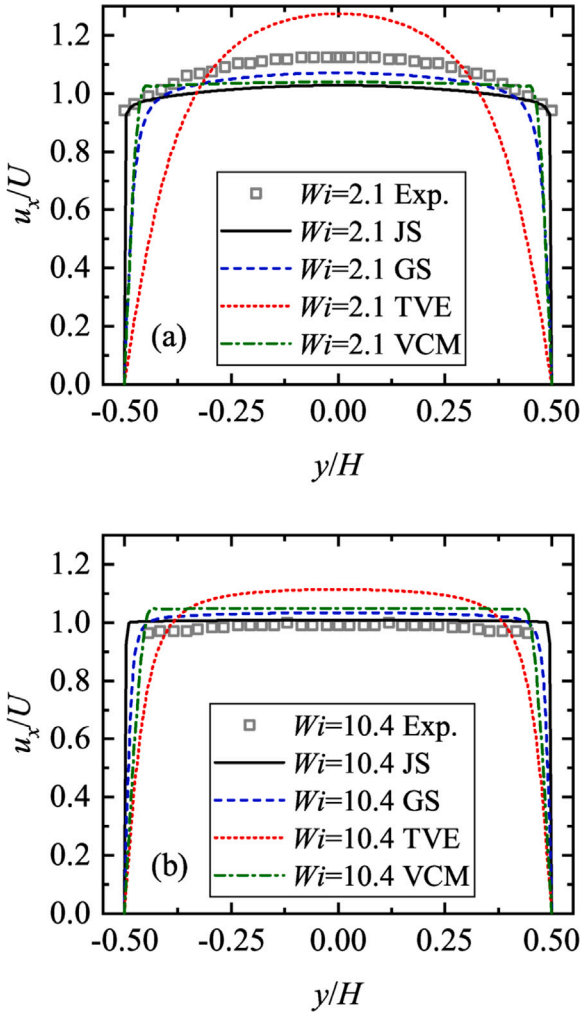


**Fig. 6.** Gapwise distribution of the $x$-component of velocity in the channel for (a) $Wi = 2.1$ and (b) $Wi = 10.4$. Comparison between experimental results [37] (symbols) and the predictions of each model.

hysteresis in simple shear (see Fig. 3), the GS model yields a smoother

transition between the bands than JS and VCM. The TVE model does not predict shear banded flow for $Wi = 2.1$ and the predicted velocity distribution for $Wi = 10.4$ is smoother than the other models. These observations are related to the stress diffusion term. Note that although $Di$ is the same among GS, TVE, and VCM, this does not mean that it has the same effect on the flow fields. The constitutive equations are highly nonlinear and the presence of diffusive terms affects significantly the interface thickness. For example, if we assign $Di = 10^{-4}$ in the TVE model, the predictions in the channel flow will match the experiment (see Appendix C). However, in order to compare the models under equal basis, we used $Di = 10^{-3}$ in all models (except for the JS, where we used $Di = 3 \cdot 10^{-3}$ because we could not solve it in mixed flows when using $Di = 10^{-3}$.

## 6. Extensional flow

The cross-slot extensional rheometer (CSER) device is designed to generate planar extensional flow in a finite region around the stagnation point at the centre of the geometry (Fig. 5(b)). It is therefore employed to probe the performance of the models under shear-free deformations. The width of the channels is $H = 200$ μm. It is well-known that the flow field in the CSER remains symmetric only for low values of the flow rate [24,25,30,98,99]. In this stable flow regime the fluid displays a localized and elongated birefringent strand extending along the outflow streamline from the stagnation point. Above a critical value of the flow rate and for negligible inertial effects, the flow bifurcates into a steady asymmetric state, where more fluid prefers to pass from the one side of the stagnation point than the other. The flow remains steady, but becomes increasingly asymmetric with increasing flow rate, eventually achieving a steady state of complete anti-symmetry characterized by a dividing streamline and birefringent strand connecting diagonally opposite corners of the cross-slot. At even higher flow rates, the flow becomes time-dependent. This pattern has been observed both in polymer solutions and WLM solutions [24,25,30,98,99]. The onset and evolution of this elastic instability can serve as an additional benchmark test for the constitutive equations because it can probe whether the constitutive models encapsulate the necessary physics to predict these asymmetric flow states.

First, we present a qualitative comparison of the stress fields when the flow is steady and symmetric. Fig. 7 illustrates a visual comparison between the measured birefringence and predicted stress profiles around the stagnation point for $Wi = 0.3$. The experimentally measured birefringence ($\Delta n$) is related to the numerically calculated principal stress difference ($\Delta\sigma$) via the stress optical rule [101]:

$$\Delta n = C_0 \Delta\sigma = C_0 \sqrt{(\tau_{xx} - \tau_{yy})^2 + 4\tau_{xy}^2}, \tag{18}$$

where $C_0$ is called the stress-optical coefficient. The value of $C_0$ for this WLM solution has been determined by Ober et al. [100] to be $C_0 = -1.1 \cdot 10^{-7}$ Pa$^{-1}$. The best qualitative prediction is achieved by GS model, because it is the only model that can reproduce the stretched hexagonal shape of the high valued stress contours around the stagnation point. The JS and the TVE models predict a diamond-like shape which does not match well with the experiment. The stress contours of the VCM model around the stagnation point exhibit a butterfly-like shape and are not even qualitatively similar to the experimental ones.

To gain a deeper insight into the predictive capability of the models, we proceed to a quantitative comparison of the predicted velocity profiles with the experimental ones. Fig. 8 presents the distribution of the dimensionless x-component of velocity ($u_x$) *versus* $x-$coordinate at the $y = 0$ plane for (a) $Wi = 0.15$ and (b) for $Wi = 0.25$. Obviously, the GS model makes a very good prediction for both flow rates, capturing precisely the slope of the velocity at the stagnation point and the overshoots for $Wi = 0.25$. The JS and TVE models underestimate the slope of the velocity for both flow rates and cannot predict the overshoots for $Wi = 0.25$. The VCM model captures the slope of the velocity for $Wi = 0.15$ and predicts the overshoots for $Wi = 0.25$, but

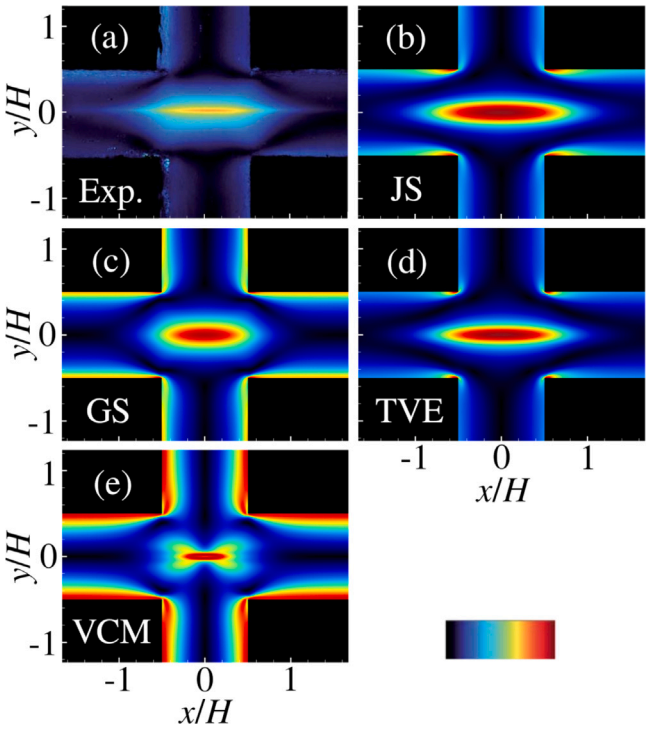


**Fig. 7.** Contours of the dimensionless principal stress difference $\Delta\sigma H/\eta_0 U$ for $Wi = 0.3$ as measured in the (a) experiment [24] and as predicted by the (b) JS, (c) GS, (d) TVE, and (e) VCM models. The experimental $\Delta\sigma$ has been calculated using Eq. (18) and $C_0 = -1.1 \cdot 10^{-7}$ Pa$^{-1}$ [100]. The colour scale represents dimensionless principal stress difference in the range 0–200 in (a), 0–50 in (b), 0–14 in (c), 0–39 in (d), and 0–14 in (e).

the extension rate is severely overestimated in the high flow rate case. Based on the comparison with the experimental data, the GS model makes the best prediction in the symmetric flow regime, followed by the TVE, JS, and VCM models.

After having evaluated the performance of the models in the symmetric flow regime, we focus on the asymmetric flow regime. In order to quantify the degree of flow asymmetry in the bifurcated flow regime, we introduce the asymmetry parameter ($I$), defined similarly to previous authors [24,25,99]:

$$I = \frac{Q_1 - Q_2}{Q_1 + Q_2}, \tag{19}$$

where $Q_1$ describes the amount of fluid that enters via one entry channel and exits via one exit channel and $Q_2$ describes the amount that enters via the same entry channel and exits via the opposite exit channel (see Fig. 5(b)). For completely symmetric flow $I = 0$ and for completely asymmetric flow $I = \pm 1$. Fig. 9(a) presents a comparison between the predictions of each model and the experimental data regarding the steady asymmetry parameter *versus* the $Wi$ number. The critical value of $Wi$ at which the flow becomes asymmetric is denoted as $Wi_{c,1}$. The last symbol or point of each line in Fig. 9(a) corresponds to the highest value of $Wi$ for which we could obtain a steady state; after that value ($Wi_{c,2}$) the flow becomes time-dependent. Fig. 9(b)-(e) presents a qualitative comparison between the experimental results and the predictions from the four constitutive models for $I = 0.4$.

Starting from the JS model, we observe that it underestimates both $Wi_{c,1}$ and $Wi_{c,2}$. However, the shape of the curve predicted by the JS model is qualitatively similar to the experiment and the maximum values of $I$ are relatively close. This underestimation of $Wi_{c,1}$ is attributed to the fact that the JS model predicts an unphysically high extensional viscosity (see Fig. 4). In turn, this leads to an increased flow resistance when compared to the experiment. Thus, the pitchfork bifurcation

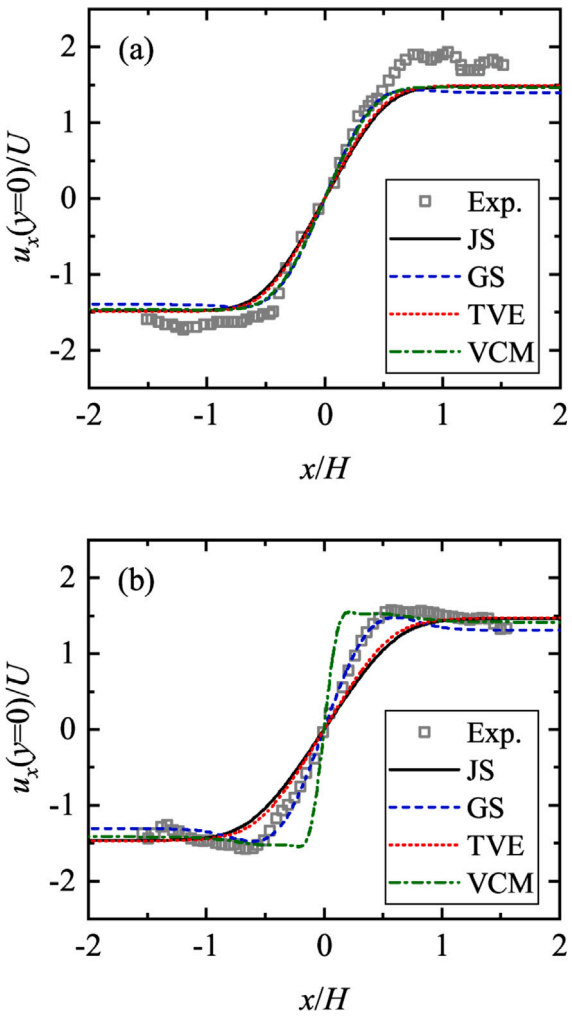


**Fig. 8.** Comparison the experimental [24] and predicted dimensionless x-component of velocity *versus* $x$−coordinate at the $y = 0$ plane for (a) $Wi = 0.15$ and (b) for $Wi = 0.25$.

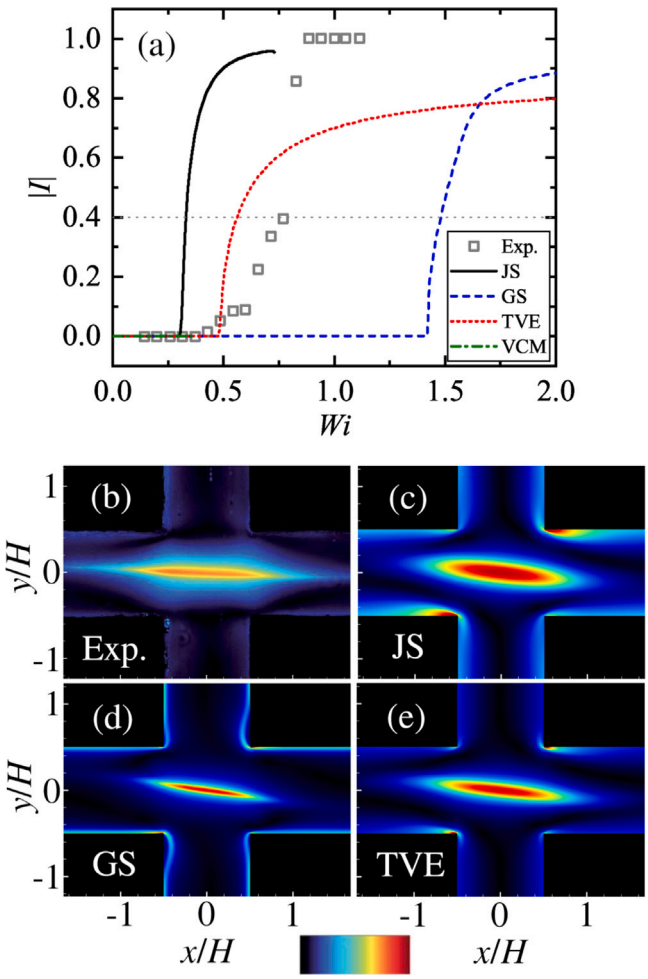


**Fig. 9.** (a) Absolute value of the steady asymmetry parameter *versus* $Wi$. Comparison between experimental results [24] (symbols) and the predictions from the four constitutive models (lines). The flow predicted by the VCM model becomes time dependent at $Wi \approx 0.355$. (b) Contours of the experimentally measured dimensionless principal stress difference $\Delta\sigma H/\eta_0 U$ for $Wi = 0.8$ and $|I| = 0.4$ [24]. The experimental $\Delta\sigma$ has been calculated using Eq. (18) and $C_0 = -1.1 \cdot 10^{-7}$ Pa$^{-1}$ [100]. Contours of the dimensionless principal stress difference $\Delta\sigma H/\eta_0 U$ for $|I| = 0.4$ as predicted by the (a) JS ($Wi = 0.33$), (b) GS ($Wi = 1.48$), and (c) TVE ($Wi = 0.56$). The colour scale represents dimensionless principal stress difference in the range 0–200 in (b), 0–50 in (c), 0–14 in (d), and 0–14 in (e).

arises at lower values of $Wi$, "relieving" the high tensile stresses around the stagnation point, and leading to shear dominated flow profiles and a lower energy state [99]. The shape of the asymmetric birefringent strand is smoother and less stretched than the one observed in the experiment.

In contrast to the JS model, the GS model overestimates $Wi_{c,1}$. Nevertheless, the shape of the curve and the maximum values of $I$ are again similar to those observed in the experiment. This overestimation of $Wi_{c,1}$ by the GS model can be explained again by the extensional viscosity (see Fig. 4); the GS model predicts weaker extension-rate hardening effects than those measured in the experimental WLM solution, and thus, $Wi_{c,1}$ is translated to higher values of $Wi$. We also have to mention that we did not find any time-dependent solutions up to $Wi = 2$ using the GS model. Despite the overprediction of $Wi_{c,1}$, the GS model gives a very good qualitative agreement regarding the contours of birefringence around the stagnation point, reproducing the asymmetric stretched hexagonal shape.

Proceeding to the TVE model, we observe a very nice agreement between the predicted and the experimental values of $Wi_{c,1}$. Although the onset of flow asymmetry is predicted at the correct value of the flow rate and the evolution of the asymmetry parameter up to $Wi \approx 0.75$ is well captured by the model, we can see a clear mismatch regarding the maximum value of $I$. The TVE model predicts a 20% lower value of $I$ than the one observed in the experiment at high values of $Wi$. Taking under consideration that the fit of the TVE model to the extensional data (see Fig. 4) is quite good, and that shear thinning promotes asymmetric states in the CSER [102], we relate this discrepancy to the inability of the TVE model to describe the strong shear thinning effects in non-homogeneous flows of this WLM solution (see Fig. 6). Moreover, the TVE model cannot predict time-dependent flow profiles up to $Wi = 2$. The TVE model gives a better prediction than the JS model regarding the distribution of the birefringence at the central region of the cross slot, but still fails to capture the shape of the experimental contours.

Finally, the VCM model, fitted to the rheology of this WLM solution, does not predict any steady asymmetric flow profiles. Instead, the flow becomes time dependent at $Wi \approx 0.355$ and a different type of flow asymmetry is observed, which is completely different from the one observed in the experiment. In this type of flow instability, the stagnation point moves periodically on the plane $y = 0$ and the flow rates at the outflow arms alternate periodically in time. Fig. 10(a) presents the outflow asymmetry parameter

$$II = \frac{Q_l - Q_r}{Q_l + Q_r}, \tag{20}$$

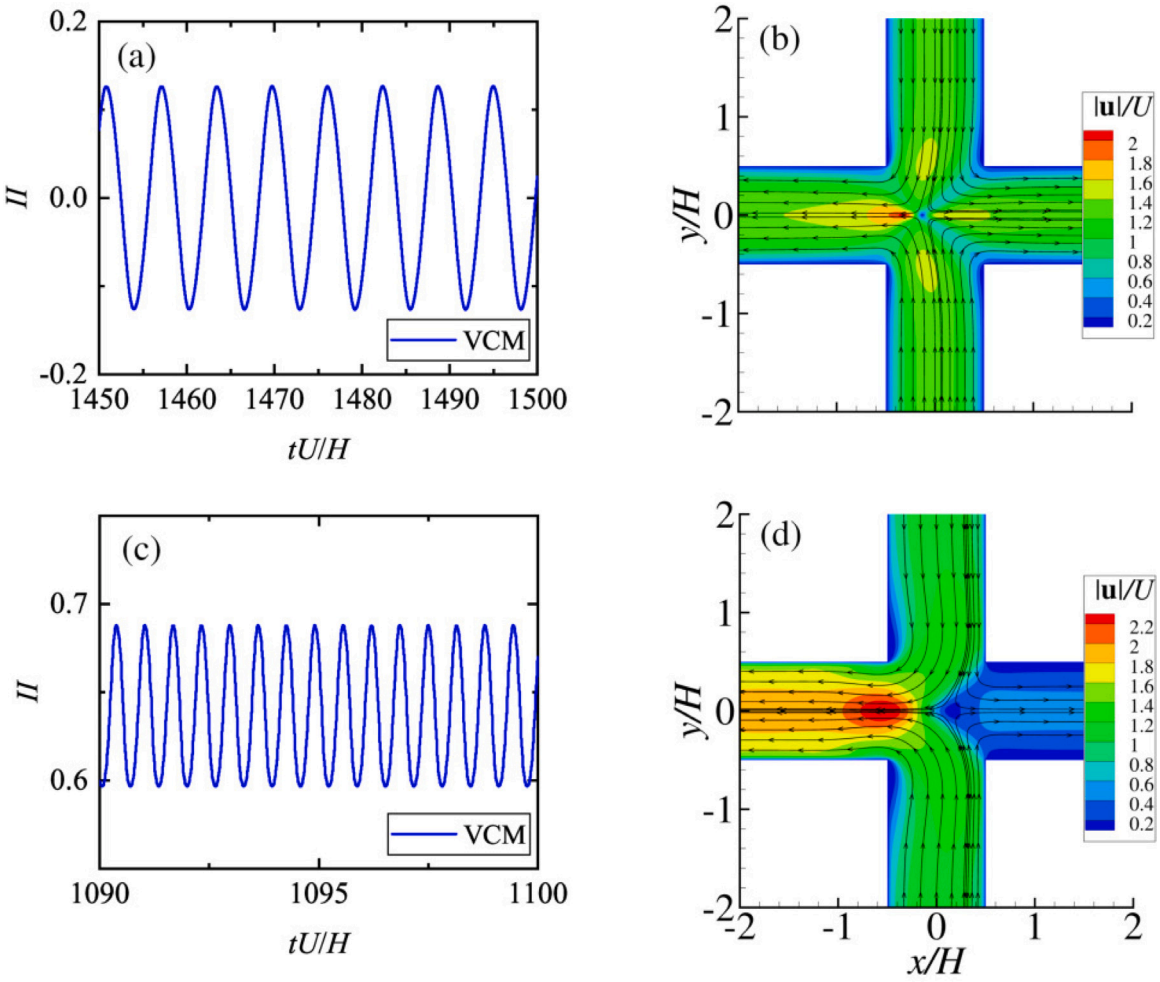


**Fig. 10.** Predictions of the VCM model in the CSER. (a) Outflow asymmetry parameter ($II$) *versus* dimensionless time ($tU/H$) for $Wi = 0.36$. (b) Contours of the dimensionless magnitude of the velocity $|\mathbf{u}|/U$ around the stagnation point with streamlines superimposed on them for $Wi = 0.36$ and $tU/H = 1471$. (c) Same as (a) but for $Wi = 0.45$. (d) Same as (b) but for $Wi = 0.45$ and $tU/H = 1095$. See also Movies 1–2.

*versus* time, where $Q_l$ and $Q_r$ are the flow rates at the left and right outflow arms, respectively. When the flow rates at both outflow arms are equal, $II = 0$, and when the fluid exits only from left(right) outflow arm, $II = +1(-1)$. As we observe, the phenomenon is purely periodic, featuring a distinct frequency. Moreover, Fig. 10(b) and Movie 1 depict contours of the magnitude of the velocity $|\mathbf{u}|$ around the stagnation point with streamlines superimposed on them. A similar type of flow instability has been observed by Haward et al. [103] in an optimized cross slot geometry [104] and by Lanzaro et al. [105] in a 3D CSER, but with dilute and semi-dilute polymer solutions, which have completely different rheological properties (mildly shear-thinning, strongly extension-hardening) than the VCM model with this set of parameters (extremely shear- and extension-thinning). For higher values of $Wi$ we observed a second type of periodic flow instability, as can be seen in Figs. 10(c)–(d) and Movie 2. The flow is still periodic and the stagnation point oscillates around the origin of axes on the plane $y = 0$, but more fluid prefers to exit from the left outflow arm than the right outflow arm. This is mirrored on the value of $II$, which attains a time averaged value around 0.64. This flow configuration can be sustained because the fluid is shear-banding; the flow in the left outflow arm is shear-banded while the flow in the right outflow arm is parabolic. Thus, the same value of the pressure can be sustained at the outflow boundaries. We also did simulations where we imposed equal flow rates between the two outflow boundaries, and observed the same type of instability, with the maxima of the velocity alternating in each outflow arm.

At first sight, one may think that our findings contradict a previous work with the VCM model in the same cross-slot geometry [54], where the authors reported steady asymmetric flow profiles, similar to those observed with the experimental WLM solution [24,25]. However, the authors in that study [54] assigned a set of parameters to the VCM model ($\mu = 2.6$, $\epsilon = 0.005$, $c_{A,0} = 1.6$, $c_{B,0} = 0.8706$, $\xi = 0.01 - 0.1$) without comparing to the experimental rheometric data of a real WLM solution. Fig. 11 presents a comparison between the predictions of the VCM model with the parameter set that we calculated by fitting the VCM model to a shear-banding WLM solution (set1) and with the parameter set assigned by Kalb et al. [54] (set2). We have also included the predictions of the Upper Convected Maxwell (UCM) model. It seems that the behaviour of the VCM model with set2 is identical to the UCM fluid in simple shear up to $\lambda\dot{\gamma} \equiv Wi_{sh} \approx 10$ and in planar extension up to $\lambda\dot{\epsilon} \equiv Wi_{ex} \approx 0.5$, explaining the observation of the steady asymmetric flow profiles. The authors [54] conclude that the reported steady asymmetric flow profiles are caused by the high extensibility of the micelles and are suppressed by the scission of the micelles. We agree with this statement and would like to add that when the instability happens ($Wi_{c,1} = 0.44$) using the VCM model with set2, the response of the fluid is very close to a UCM fluid. Observing Fig. 11, some flow curves, and extensional data for both non-shear-banding and shear-banding WLM solutions [25], we can realize that the VCM model with set2 does not represent a shear-banding WLM solution, but instead it could represent a semi-dilute polymer solution. When Kalb et al. [54] used the VCM model with set2 and $\xi = 0.1$, which is somewhat closer

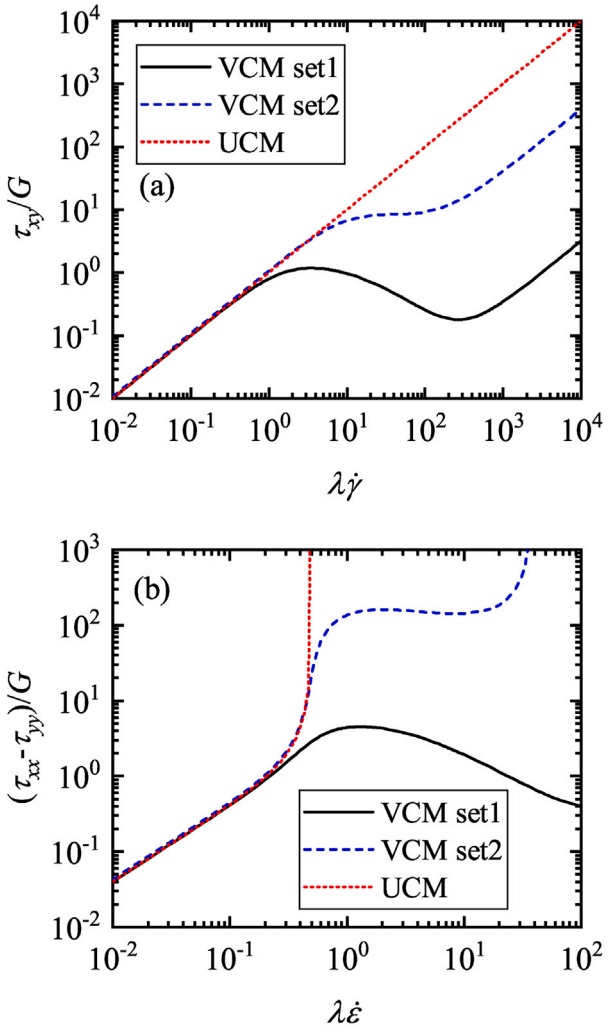


**Fig. 11.** (a) Shear stress *versus* shear rate in simple shear for the VCM model with the parameter set used in this study (set1), the parameter set used in [54] (set2), and for the UCM model. (b) Tensile stress difference *versus* extension rate in planar extension for the VCM model with the parameter set used in this study (set1), the parameter set used in [54] (set2), and for the UCM model.

to a real WLM solution (less extension-rate hardening), they could not find the steady asymmetric states. Additionally, when we use the VCM model with a parameter set that describes a real shear-banding WLM solution, the steady instability does not arise at all. Instead, we get a different type of flow instability (Fig. 10) from that observed in the experiment and predicted by the other three models. We believe that this discrepancy in the VCM model is related to the extreme extension-rate thinning that it predicts (Figs. 4, 11) when it is fitted to a shear-banding WLM solution. In fact, the tensile stress difference in extension becomes non-monotonic (Fig. 11(b)); this means that the flow resistance decreases as we increase the flow rate in the CSER, stong extensional stresses do not build up around the stagnation point, and the steady asymmetric instability is suppressed. This argument is in line with the findings of Kordalis et al. [106] who reported that they could not find the steady asymmetry in the CSER with elasto-visco-plastic fluids that do not exhibit extension-rate hardening. In the same trend, Cromer et al. [58] performed filament stretching simulations with the VCM model and a parameter set that corresponds to a shear banding WLM solution and reported the absence of an elastocapillary thinning regime. Instead, they observed an elastic rupture of the filament, which was attributed to the breakage of the micelles and the pronounced extensional thinning response. Furthermore, the onset of periodic elastic instabilities was recently linked with strong extension-rate thinning effects [107], something that could also apply in the present case with the VCM model. At this point we have to mention that the Germann–Cook–Beris (GCB) variant [80] of the VCM model suffers from the same problem: it cannot predict shear-banding without also predicting a strongly non-monotonic tensile stress difference in extension. A possible solution could be to adopt a different expression for the breakage rate of species A that would resolve this problem, but this is a separate project that could be addressed in a future study.

One may wonder why the TVE model is so much better than the VCM model at predicting the flow in the CSER, despite the extensional flow curves (see Fig. 4) being rather similar. This happens because the TVE predicts strong overshoots in the startup extensional viscosity, which can enhance flow resistance and trigger the flow asymmetry. A detailed explanation is given in Appendix D.

To conclude with this section we find that the GS model yields the best prediction in the symmetric flow regime, followed by the TVE, JS, and VCM models. In the asymmetric regime, the TVE model performs best, followed by the JS and GS models. Only the JS model can predict the transition to the time-dependent regime. The VCM model cannot predict the steady asymmetric flow regime.

## 7. Mixed flow

After investigating the behaviour of the models in shear and extensional flows, we now examine the case where a combination of both shearing and extensional deformations influence the rheological properties of the micelles in the fluid. In analogy to the benchmark experiment of the flow around a sphere, we employ a microfluidic cylinder [37]. The flow past a cylinder generates strong compressional and extensional kinematics upstream and downstream of the cylinder, respectively, with strong shearing flow around the sides of the cylinder. The most important geometrical characteristic of the flow past a cylinder in a channel is the blockage ratio $B_R = 2R/H$. The flow in microchannels with high $B_R$ resembles a constriction flow, because it is dominated by compressional deformations around the upstream stagnation point of the cylinder. At the other limit, the flow in microchannels with low $B_R$ is dominated by extensional deformations and long residence times around the downstream stagnation point of the cylinder. The effect of the blockage ratio on the flow kinematics can also be related to two different types of elastic instabilities that have been observed in creeping flows of WLM solutions around microfluidic cylinders: (1) the onset of time dependent flow, accompanied by upstream vortices in channels with high blockage ratio [36], and (2) the onset of characteristic steady flow asymmetry, with more fluid choosing to pass from the one side of the cylinder, in channels with low blockage ratio [37]. Note that the second type of elastic instability has also been observed in polymer solutions and has been related to the interplay of elasticity and shear-thinning [108–110]. In this study we will focus on the later case, and more specifically, we will test the constitutive models in a microfluidic cylinder device with $B_R = 0.1$. The dimensions of the microchannel are $H = 400\ \mu m$ and $R = 20\ \mu m$.

First, we present a visual comparison of the velocity fields when the flow is steady and symmetric. Fig. 12 illustrates a qualitative comparison between the measured and predicted velocity profiles around the cylinder for $Wi = 3.75$. The experimental velocity profiles were measured using particle image velocimetry (PIV). For the comparison with the experimental data, we had to normalize the calculated velocities with the maximum value of the velocity magnitude $|\mathbf{u}|_{max}$, which is different for each model ($|\mathbf{u}|_{max,JS}/U = 1.579$, $|\mathbf{u}|_{max,GS}/U = 1.358$, $|\mathbf{u}|_{max,TVE}/U = 1.627$). The GS model makes the best prediction in the steady and symmetric flow regime; it is the only model that can predict correctly the shape of the low-velocity contours around the cylinder and also downstream of the cylinder. The JS and the TVE models cannot capture these trends, yielding qualitatively different velocity contours, especially at the low-velocity region close to the cylinder.

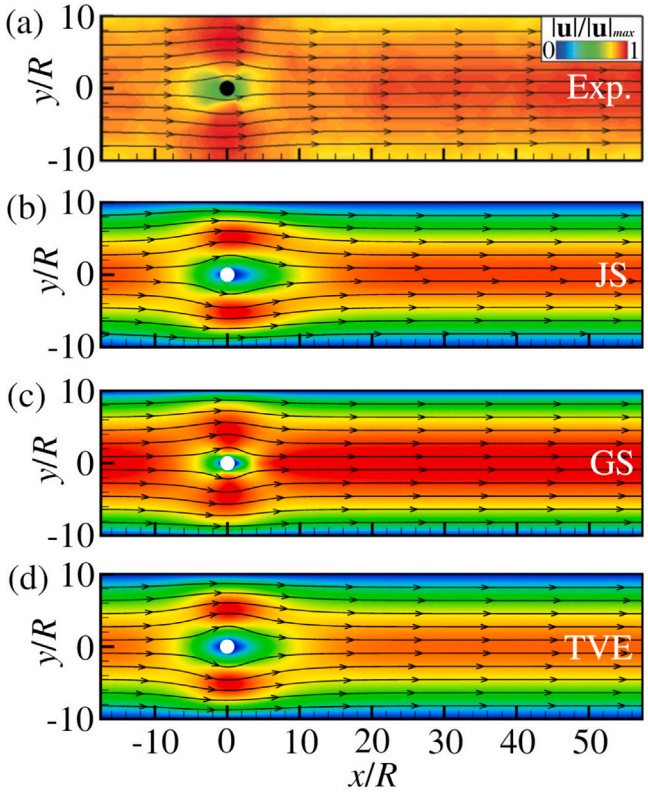


**Fig. 12.** Contours of the dimensionless velocity magnitude $U_m = |\mathbf{u}|/|\mathbf{u}|_{max}$ for $Wi = 3.75$. (a) Experiment [37], (b) JS, (c) GS, (d) TVE. The VCM model does not predict a steady state for $Wi = 3.75$.

We do not present contours for the VCM model because it does not predict a steady state; instead, it predicts a transient flow state for $Wi = 3.75$ (Movie 3). Subsequently, we proceed to a quantitative comparison of the flow profiles for $Wi = 3.75$. Fig. 13 presents a quantitative comparison of the scaled $x-$component of the velocity at the sides of the cylinder ($x = 0$) *versus* the $y-$coordinate. As expected by the qualitative comparison, the prediction by the GS models is closer to the experimental data; it can predict very nicely the velocity profile close to the cylinder, but fails to describe the plug-like velocity profile near the walls. However, this is equally likely to be a failure of the PIV experiment; in PIV measurements it is very difficult to resolve very close to the boundaries. The JS and the TVE models yield similar parabolic-like velocity distributions, with the former predicting a sharper boundary layer in the velocity close to the cylinder. Once again, the GS model performs best in the symmetric flow regime.

Finally, we proceed to the last benchmark test for the constitutive models: the capability to predict the elastic instability in the flow past a cylinder in a channel. As shown by Haward et al. using the present model WLM solution [37], this instability, which is steady in time over a range of $Wi > Wi_{c,1}$, is characterized by the preferential passage of fluid around one side of the cylinder (i.e., a lateral asymmetry of the flow field). Moreover, it has been proven to be a supercritical pitchfork bifurcation with a random selection of the preferred side of passage [108,109]. In some cases, the degree of asymmetry is so extreme that all the fluid is observed to pass on only one side of the cylinder, with a region of stagnant fluid developing on the opposite side. As in the CSER, the flow becomes time dependent at higher values of $Wi > Wi_{c,2}$. The asymmetry parameter ($I^*$) will be employed to quantify the flow asymmetry in the microchannel:

$$I^* = \frac{u_x|_{x=0,y/R=5.5} - u_x|_{x=0,y/R=-5.5}}{u_x|_{x=0,y/R=5.5} + u_x|_{x=0,y/R=-5.5}}, \tag{21}$$

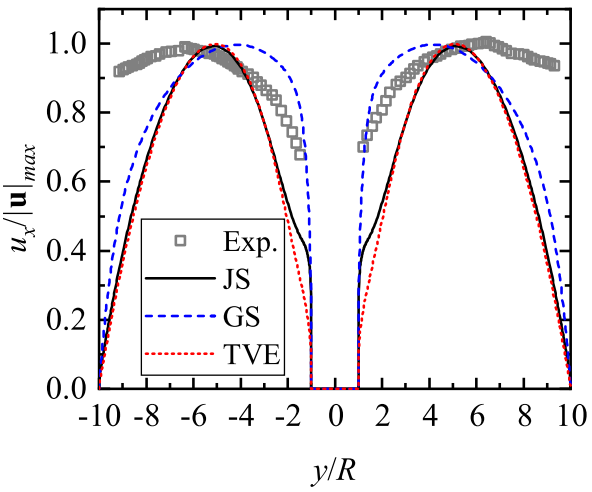


**Fig. 13.** Distribution of the dimensionless $x-$component of the velocity at the sides of the cylinder ($x = 0$) *versus* the $y-$coordinate for $Wi = 3.75$. (a) Experiment [37], (b) JS, (c) GS, (d) TVE. The VCM model does not predict a steady state for $Wi = 3.75$.

which compares the values of the streamwise velocities at each side of the cylinder, calculated at the mid-distance between the cylinder and the walls of the channels.

Fig. 14 illustrates the exact same pattern observed in the CSER. The JS and GS models predict the correct shape of the curve but underestimate and overestimate $Wi_{c,1}$, respectively. The TVE model makes the best prediction regarding $Wi_{c,1}$ but underestimates the degree of flow asymmetry at higher values of $Wi$. The GS model achieves the best qualitative match of the dimensionless magnitude of velocity (see Figs. 14(b)–(d)). The VCM model does not predict steady asymmetric profiles; instead, the flow becomes time dependent at $Wi \approx 2.1$, the flow variables vary periodically in time, the stresses pulsate at the wake of the cylinder, but the flow field remains laterally symmetric (see Movie 3). Note that Khan and Sasmal [56] have found this instability using the VCM model, but they were using the same set of parameters as Kalb et al. [54], which does not correspond to a real shear-banding WLM solution (see Fig. 11 and Section 6). Keeping in mind that both extension-rate hardening and shear-thinning promote the asymmetric flow states [108–110], these observations can be justified by the same arguments that we used in the CSER. The JS model is extremely strain-hardening, triggering the instability at very low values of $Wi$. The TVE model is more extension-hardening than the GS model, thus, the instability arises at lower values of $Wi$. However, the fact that the TVE model is less shear-thinning than the GS model leads to a smoother evolution of $I$ *versus* $Wi$. Ultimately, the breakage of the micelles, predicted by the VCM model, prevents stretch and the development of strong tensile stresses, thus, suppressing the instability.

To sum up with the flow past a cylinder in a channel, we find that the GS model yields the best prediction in the symmetric flow regime, followed by the TVE, JS, and VCM models. In the asymmetric regime, the TVE model performs best, followed by the JS and GS models. The VCM model predicts time dependent flow profiles at very low values of $Wi$ and cannot predict the steady asymmetric flow regime.

## 8. Summary and conclusions

We investigated the performance of four constitutive models for shear-banding WLM solutions by directly comparing their predictions with existing experimental data. All the models were first calibrated to a strongly shear-banding WLM solution, under SAOS, simple shear and steady planar elongation. The conclusions of our analysis may be summarized as follows:

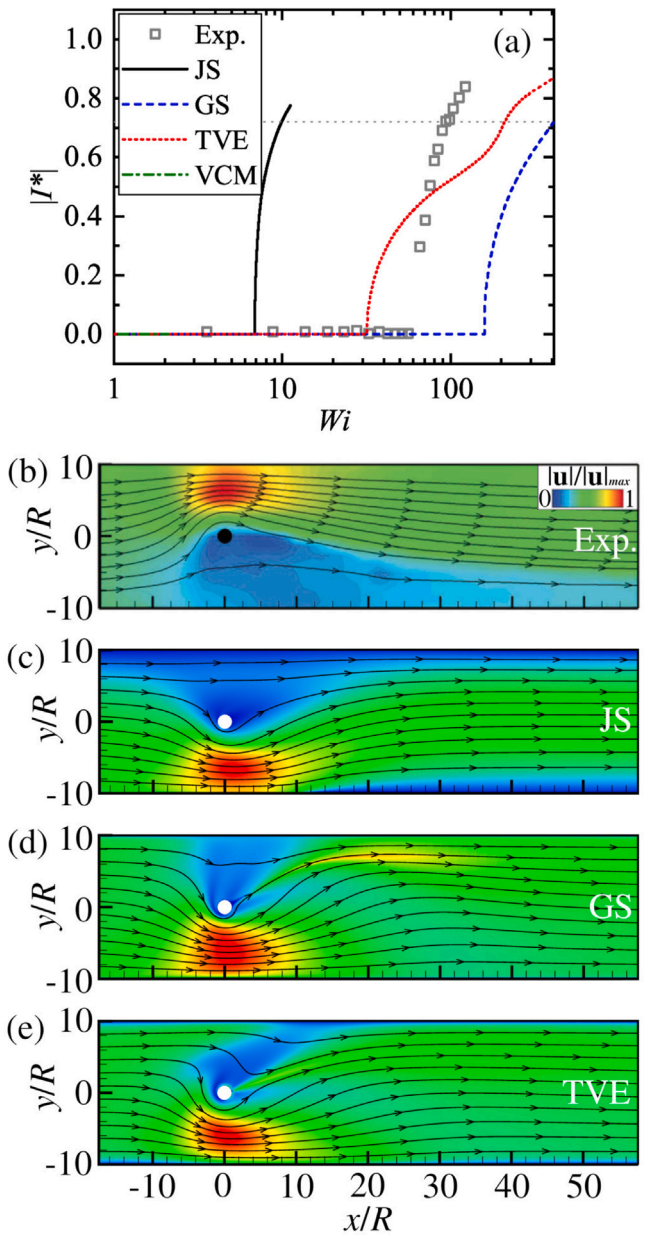


**Fig. 14.** (a) Absolute value of the steady asymmetry parameter *versus* $Wi$. Comparison between experimental results [37] (symbols) and each model's predictions (lines). The flow predicted by the VCM model becomes time dependent at $Wi \approx 2.1$. (b) Contours of the experimental dimensionless velocity magnitude $U_m = |\mathbf{u}|/|\mathbf{u}|_{max}$ for $Wi = 93.8$ and $|I^*| = 0.72$ [37]. Contours of the dimensionless velocity magnitude $U_m = |\mathbf{u}|/|\mathbf{u}|_{max}$ for $|I^*| = 0.72$ as predicted by the (a) JS ($Wi = 10$), (b) GS ($Wi = 410$), and (c) TVE ($Wi = 211$).

- The JS, GS, and VCM models yielded quantitative agreement regarding the shear-banded velocity profiles in the planar Poiseuille flow. The TVE model did not capture correctly the plug-like flow profiles.
- In the extension-dominated flow in the CSER, we found that the GS and TVE models yielded the best predictions in the symmetric and asymmetric regimes, respectively. The JS model made only qualitative predictions in the CSER. The VCM model did not predict the correct flow profiles when it was adjusted to the rheology of the model WLM solution; one could find a set of parameters for the VCM that would yield steady asymmetric flow profiles in the CSER, but these parameters would not correspond to the rheological fingerprint of shear-banding WLM solutions.
- The models displayed the same trends in the flow past a cylinder in a channel: the GS and TVE models gave the best description of the symmetric and asymmetric flow regimes, respectively. The JS model provided only qualitative predictions of the flow. The VCM model did not agree with the experimental data, predicting a different type of elastic instability, which has not been observed in experiments with WLM solutions.
- Regarding numerical stability, we encountered divergence of the numerical scheme only when the JS model was predicting time-dependent solutions.

Based on the overall performance of the models and also accounting for the factor of simplicity, our results point to the GS model as the current best candidate for CFD simulations of shear-banding WLM solutions. However, the GS model cannot provide a complete picture of the microscopic and mesoscopic physics of WLMs. On the other hand, the VCM model encapsulates realistic physical mechanisms but these seem to apply only in shear flows. The VCM model makes correct predictions in rheometric (where the flow field is imposed) and inhomogeneous purely shear flows but fails to predict the correct trends in mixed flows, where the flow interacts with the material properties. Based on our analysis, this happens because the VCM model underpredicts extension hardening effects. A possible explanation could be that the rate of micelle breakage is different in shear and extension. Current models assume that the micelle breakage ratio is proportional to a scalar quantity, namely the double dot product of the stress and deformation rate tensors. A model that would incorporate a micelle breakage ratio that depends also on the flow type and direction (something proportional to kinematic hardening) could potentially solve this problem. However, new experiments and molecular or mesoscopic simulations are necessary to validate this assumption. We must note that recent population balance-based constitutive equations do not predict non-monotone extension curves [48]. To conclude, the reported quantitative mismatch between the models and the experiment stresses the necessity for adjustments in existing models, or the derivation of new ones, which will be capable of predicting more accurately the rheological response of shear-banding WLM solutions.

## Declaration of competing interest

The authors declare that they have no known competing financial interests or personal relationships that could have appeared to influence the work reported in this paper.

## Data availability

Data will be made available on request.

## Acknowledgements

SV, SJH, CCH, and AQS gratefully acknowledge the support of the Okinawa Institute of Science and Technology Graduate University (OIST) with subsidy funding from the Cabinet Office, Government of Japan, and also funding from the Japan Society for the Promotion of Science (JSPS, Grant Nos. 20K14656 and 21K03884) and the Joint Research Projects (JRPs) supported by the JSPS and the Swiss National Science Foundation (SNSF). JT has been supported financially by the Hellenic Foundation of Research and Innovation, Greece, grant HFRI FM17-2309 MOFLOWMAT. The authors are grateful for the help and support provided by the Scientific Computing and Data Analysis section of Research Support Division at OIST.

**Table B.2**
Main characteristics of the meshes used in the CSER.

| Mesh | Element size $h_e/H$ | No. of triangles | No. of nodes |
|---|---|---|---|
| M1 | 0.014 | 41200 | 20857 |
| M2 | 0.007 | 166400 | 83817 |
| M3 | 0.0035 | 668800 | 335437 |

## Appendix A. Modified Bautista–Manero (MBM) model

The set of equations, expressed in terms of the conformation tensor, are given as:

$$\overset{\triangledown}{\mathbf{C}} + G\phi(\mathbf{C}-\mathbf{I}) = 0, \tag{A.1}$$

$$\frac{D\phi}{Dt} = \left(\frac{1}{G\lambda^2} - \frac{\phi}{\lambda}\right) - k_0(1+\mu|\dot{\gamma}|)(\phi-\phi_\infty)(\dot{\boldsymbol{\gamma}} : \mathbf{C}), \tag{A.2}$$

where $\phi$ is the fluidity parameter and $k_0$, $\mu$, and $\phi_\infty$ are adjustable parameters of the model [74].

## Appendix B. Mesh convergence study

Fig. B.15 illustrates the effect of mesh refinement (a) on the fully developed velocity profile at the lower inflow arm ($y/H = -0.5$) and (b) on the asymmetry parameter ($|I|$) for the GS fluid (see Table 1) in the CSER. The mesh convergence test was performed by solving the flow in three different meshes, whose characteristics are given in Table B.2. M2 and M3 are generated by sequentially doubling the elements of M1 in each direction. Mesh M2 was used in all simulations in the CSER.

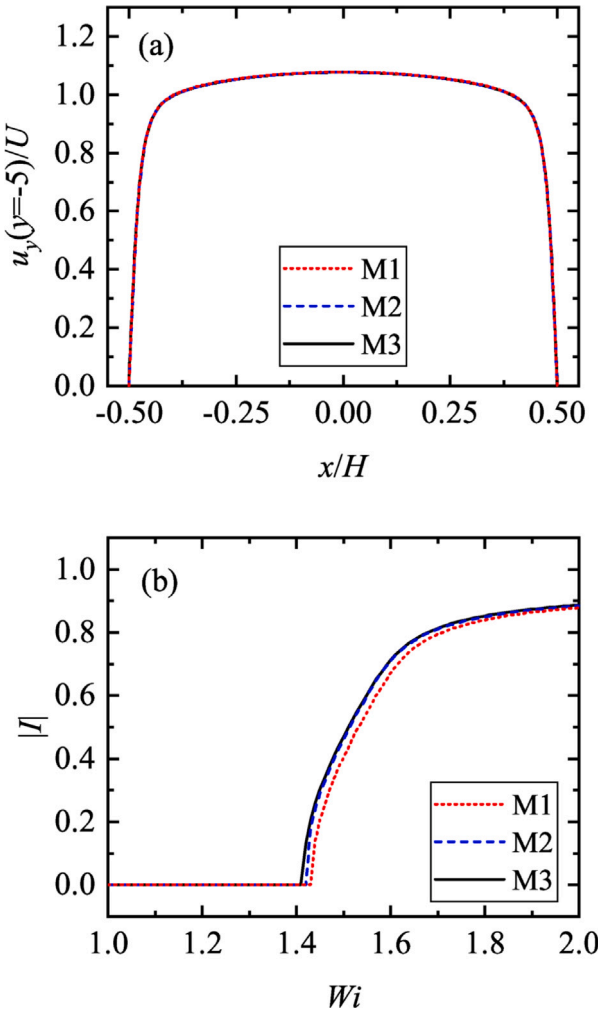


**Fig. B.15.** The effect of mesh refinement on (a) the fully developed velocity profile at the lower inflow arm and (b) the asymmetry parameter for the GS fluid in the CSER.

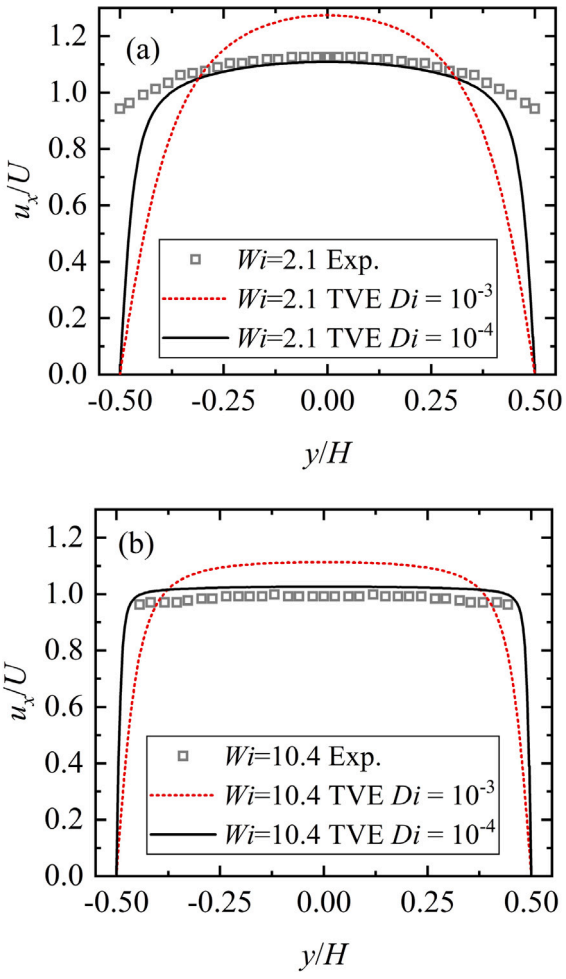


**Fig. C.16.** Predictions of the TVE model in the channel flows for different values of $Di$.

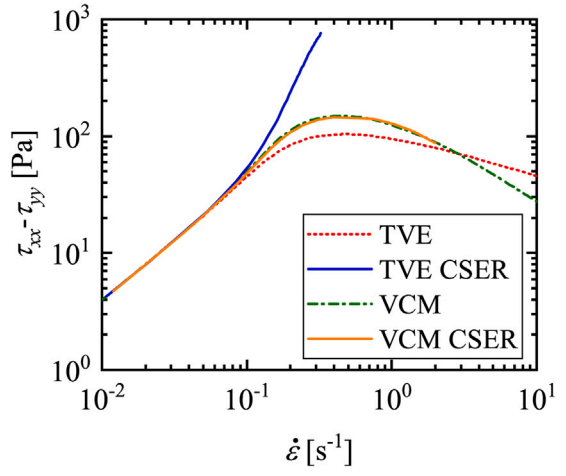


**Fig. D.17.** Comparison of the homogeneous extension curves and the tensile stress difference versus the extension rate, measured from the 2D simulations in the CSER, for the TVE and VCM models.

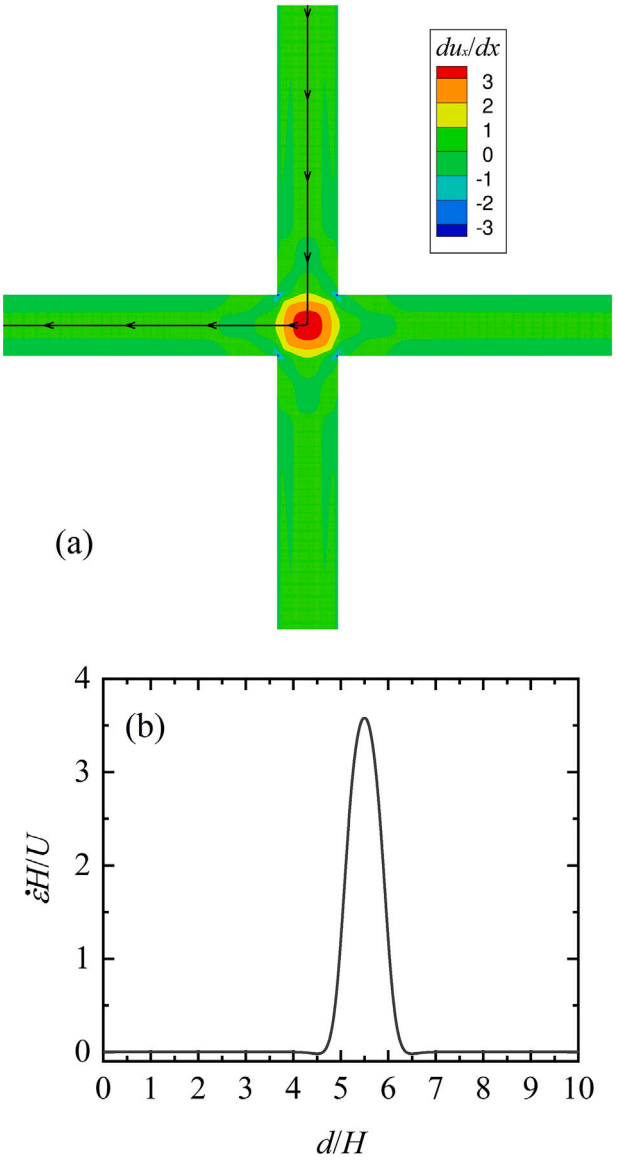


**Fig. D.18.** (a) Streamline located close to the stagnation point, superimposed to contours of $\partial u_x/\partial x$ for creeping Newtonian flow. (b) Extension rate as a function of the arclength, d, along the streamline.

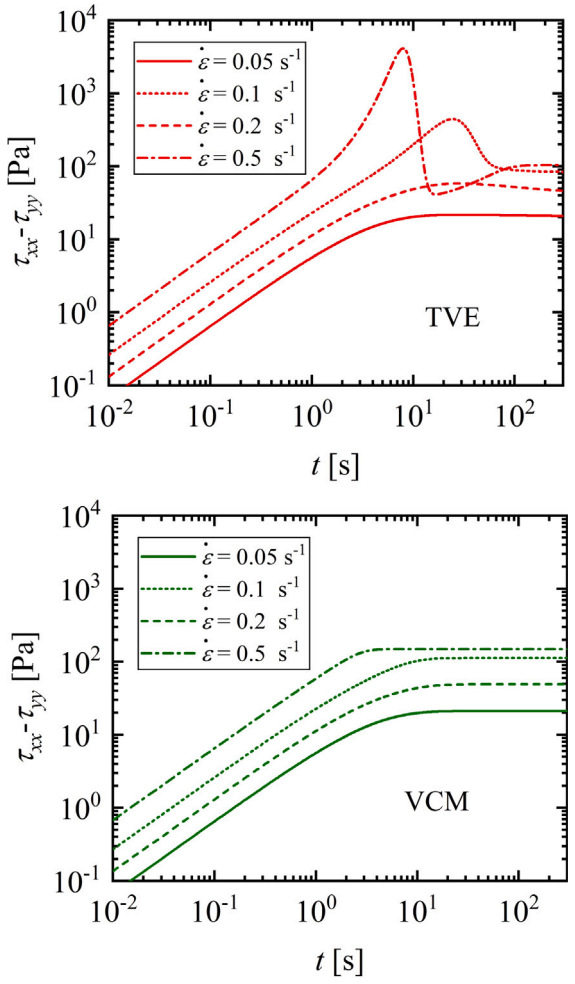


**Fig. D.19.** Tensile stress difference *versus* time for startup of homogeneous planar extension.

A mesh convergence study for the flow past a cylinder in a straight channel can be found in [109]. Here, we used a mesh with element size $h_e/R = 0.007$ on the cylinder surface and the walls of the channel for all the simulations in Section 7.

## Appendix C. TVE model predictions in channel flow with $Di = 10^{-4}$

The TVE model does not predict shear banded flow for $Wi = 2.1$ and the predicted velocity distribution for $Wi = 10.4$ is smoother than the rest of the models. These observations are related to the stress diffusion term. Note that although $Di$ is the same among GS, TVE, and VCM, this does not mean that it has the same effect on the flow fields. The constitutive equations are highly nonlinear and the presence of diffusive terms affects significantly the interface thickness. For example, if we assign $Di = 10^{-4}$ in the TVE model, the predictions in the channel flow will match the experiment (see Fig. C.16). However, in order to compare the models under equal basis, we used $Di = 10^{-3}$ in all models (except for the JS, where we used $Di = 3 \cdot 10^{-3}$ because we could not solve it in mixed flows when using $Di = 10^{-3}$).

## Appendix D. Difference between TVE and VCM models in the CSER

Fig. D.17 compares the homogeneous extension curves and the tensile stress difference versus the extension rate, measured from the 2D simulations in the CSER, for the TVE and VCM models. Note that the curves from the CSER stop when the flow becomes asymmetric. Regarding the VCM model, a good agreement is reached between the homogeneous extension curve and the measurements from the CSER. As explained in the manuscript, this extension thinning response suppresses the asymmetry and instead leads to time-dependent flow. However, we observe a striking difference between the curves in the case of the TVE model. The measurement from the CSER reveals a strong strain-hardening response that can justify the onset of asymmetry but does not match the homogeneous curve.

To understand why this happens, we must follow the path of a fluid parcel that enters the CSER and flows very close to the stagnation point, as seen in Fig. D.18(a). While the parcel flows in the arm of the CSER, it experiences negligible shear rates because it is located close to the symmetry plane, where the shear rate is zero. As the parcel approaches the stagnation point, it feels an increase in the extension rate. The experienced extension rate maximizes next to the stagnation point and decreases to zero as the parcel heads to the exit of the outflow arm.

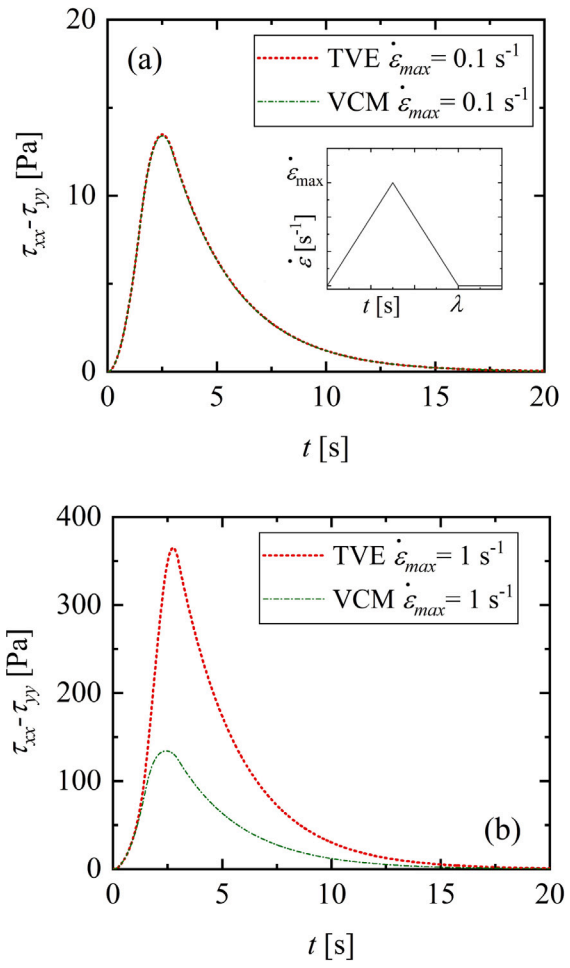


**Fig. D.20.** Tensile stress difference *versus* time for homogeneous planar extension, imposing a triangular step in the extension rate for the TVE and VCM models.

Fig. D.18(b) quantifies this effect by plotting the extension rate as a function of the arclength along the streamline.

The flow is steady in the Eulerian description but is always transient in the Lagrangian description. Consequently, startup planar extension (followed by cessation) is the most relevant material function to the deformation history of the fluid parcel. Fig. D.19 plots the startup tensile stress differences for the TVE and VCM models at different extension rates. The TVE model predicts strong overshoots in the tensile stresses that are not predicted by the VCM model at these extension rates. This causes the difference between the homogeneous extension curves and those measured in the CSER, and is what extension curves and triggers the flow asymmetry.

To further verify our explanation, we solved the TVE and VCM models in homogeneous planar extension, imposing a triangular step in the extension rate for various extension rates (Fig. D.20). For low extension rates, both models predict the same response. However, at higher extension rates, the TVE model predicts strong extension-hardening which is caused by the overshoots discussed above. The same happens around the downstream stagnation point in the flow past the cylinder. To conclude with this matter, we have shown that extension-hardening in the TVE model comes from the overshoots in the extensional response and the asymmetric flow states can be predicted.

## References


[1] S.J. Haward, A.Q. Shen, Microfluidic flows and confinement of wormlike micelles: advances in systems, characterization, and applications, in: Wormlike Micelles, Royal Society of Chemistry, 2017, pp. 236–278.

[2] J.N. Israelachvili, Intermolecular and Surface Forces, Academic Press, 2015.

[3] J.-F. Berret, Rheology of wormlike micelles: Equilibrium properties and shear banding transitions, in: Molecular Gels, Springer, 2006, pp. 667–720.

[4] R.G. Larson, The Structure and Rheology of Complex Fluids, Vol. 150, Oxford University Press, New York, 1999.

[5] M.E. Cates, Reptation of living polymers: dynamics of entangled polymers in the presence of reversible chain-scission reactions, Macromolecules 20 (9) (1987) 2289–2296, http://dx.doi.org/10.1021/ma00175a038.

[6] T. Shikata, S.J. Dahman, D.S. Pearson, Rheo-optical behavior of wormlike micelles, Langmuir 10 (10) (1994) 3470–3476, http://dx.doi.org/10.1021/la00022a019.

[7] F. Nettesheim, N.J. Wagner, Fast dynamics of wormlike micellar solutions, Langmuir 23 (10) (2007) 5267–5269, http://dx.doi.org/10.1021/la0635855.

[8] M.E. Cates, S.J. Candau, Statics and dynamics of worm-like surfactant micelles, J. Phys.: Condens. Matter 2 (33) (1990) 6869, http://dx.doi.org/10.1088/0953-8984/2/33/001.

[9] J. Appell, G. Porte, A. Khatory, F. Kern, S. Candau, Static and dynamic properties of a network of wormlike surfactant micelles (cetylpyridinium chlorate in sodium chlorate brine), J. Phys. II 2 (5) (1992) 1045–1052, http://dx.doi.org/10.1051/jp2:1992104.

[10] S.J. Candau, R. Oda, Linear viscoelasticity of salt-free wormlike micellar solutions, Colloids Surf. A 183 (2001) 5–14, http://dx.doi.org/10.1016/S0927-7757(01)00535-0.

[11] T.S. Davies, A.M. Ketner, S.R. Raghavan, Self-assembly of surfactant vesicles that transform into viscoelastic wormlike micelles upon heating, J. Am. Chem. Soc. 128 (20) (2006) 6669–6675, http://dx.doi.org/10.1021/ja060021e.

[12] S.R. Raghavan, Distinct character of surfactant gels: a smooth progression from micelles to fibrillar networks, Langmuir 25 (15) (2009) 8382–8385, http://dx.doi.org/10.1021/la901513w.

[13] S. Kefi, J. Lee, T. Pope, P. Sullivan, E. Nelson, A. Hernandez, T. Olsen, M. Parlar, B. Powers, A. Roy, et al., Expanding applications for viscoelastic surfactants, Oilfield Rev. 16 (4) (2004) 10–23.

[14] H. Rehage, H. Hoffmann, Viscoelastic surfactant solutions: model systems for rheological research, Mol. Phys. 74 (5) (1991) 933–973, http://dx.doi.org/10.1080/00268979100102721.

[15] M.S. Turner, M.E. Cates, Linear viscoelasticity of wormlike micelles: a comparison of micellar reaction kinetics, J. Phys. II 2 (3) (1992) 503–519, http://dx.doi.org/10.1051/jp2:1992102.

[16] C. Perge, M.-A. Fardin, S. Manneville, Surfactant micelles: Model systems for flow instabilities of complex fluids, Eur. Phys. J. E 37 (4) (2014) 1–12, http://dx.doi.org/10.1140/epje/i2014-14023-4.

[17] G. Porte, J.-F. Berret, J.L. Harden, Inhomogeneous flows of complex fluids: Mechanical instability versus non-equilibrium phase transition, J. Phys. II 7 (3) (1997) 459–472, http://dx.doi.org/10.1051/jp2:1997138.

[18] P.A. Vasquez, G.H. McKinley, L.P. Cook, A network scission model for wormlike micellar solutions: I. Model formulation and viscometric flow predictions, J. Non-Newton. Fluid Mech. 144 (2–3) (2007) 122–139, http://dx.doi.org/10.1016/j.jnnfm.2007.03.007.

[19] Y.T. Hu, A. Lips, Kinetics and mechanism of shear banding in an entangled micellar solution, J. Rheol. 49 (5) (2005) 1001–1027, http://dx.doi.org/10.1122/1.2008295.

[20] E. Miller, J.P. Rothstein, Transient evolution of shear-banding wormlike micellar solutions, J. Non-Newton. Fluid Mech. 143 (1) (2007) 22–37, http://dx.doi.org/10.1016/j.jnnfm.2006.12.005.

[21] J.-B. Salmon, A. Colin, S. Manneville, F. Molino, Velocity profiles in shear-banding wormlike micelles, Phys. Rev. Lett. 90 (22) (2003) 228303, http://dx.doi.org/10.1103/PhysRevLett.90.228303.

[22] R.K. Prud'homme, G.G. Warr, Elongational flow of solutions of rodlike micelles, Langmuir 10 (10) (1994) 3419–3426, http://dx.doi.org/10.1021/la00022a010.

[23] J.P. Rothstein, Transient extensional rheology of wormlike micelle solutions, J. Rheol. 47 (5) (2003) 1227–1247, http://dx.doi.org/10.1122/1.1603242.

[24] S.J. Haward, T.J. Ober, M.S.N. Oliveira, M.A. Alves, G.H. McKinley, Extensional rheology and elastic instabilities of a wormlike micellar solution in a microfluidic cross-slot device, Soft Matter 8 (2) (2012) 536–555, http://dx.doi.org/10.1039/C1SM06494K.

[25] S.J. Haward, G.H. McKinley, Stagnation point flow of wormlike micellar solutions in a microfluidic cross-slot device: Effects of surfactant concentration and ionic environment, Phys. Rev. E 85 (3) (2012) 031502, http://dx.doi.org/10.1103/PhysRevE.85.031502.

[26] A. Jayaraman, A. Belmonte, Oscillations of a solid sphere falling through a wormlike micellar fluid, Phys. Rev. E 67 (6) (2003) 065301, http://dx.doi.org/10.1103/PhysRevE.67.065301.

[27] S. Chen, J.P. Rothstein, Flow of a wormlike micelle solution past a falling sphere, J. Non-Newton. Fluid Mech. 116 (2–3) (2004) 205–234, http://dx.doi.org/10.1016/j.jnnfm.2003.08.005.

[28] H. Mohammadigoushki, S.J. Muller, Sedimentation of a sphere in wormlike micellar fluids, J. Rheol. 60 (4) (2016) 587–601, http://dx.doi.org/10.1122/1.4948800.

[29] J.A. Pathak, S.D. Hudson, Rheo-optics of equilibrium polymer solutions: Wormlike micelles in elongational flow in a microfluidic cross-slot, Macromolecules 39 (25) (2006) 8782–8792, http://dx.doi.org/10.1021/ma061355r.

[30] N. Dubash, P. Cheung, A.Q. Shen, Elastic instabilities in a microfluidic cross-slot flow of wormlike micellar solutions, Soft Matter 8 (21) (2012) 5847–5856, http://dx.doi.org/10.1039/C2SM25215E.

[31] M.-A. Fardin, D. Lopez, J. Croso, G. Grégoire, O. Cardoso, G.H. McKinley, S. Lerouge, Elastic turbulence in shear banding wormlike micelles, Phys. Rev. Lett. 104 (17) (2010) 178303, http://dx.doi.org/10.1103/PhysRevLett.104.178303.

[32] M.-A. Fardin, L. Casanellas, B. Saint-Michel, S. Manneville, S. Lerouge, Shear-banding in wormlike micelles: Beware of elastic instabilities, J. Rheol. 60 (5) (2016) 917–926, http://dx.doi.org/10.1122/1.4960333.

[33] S.M. Fielding, P.D. Olmsted, Nonlinear dynamics of an interface between shear bands, Phys. Rev. Lett. 96 (10) (2006) 104502, http://dx.doi.org/10.1103/PhysRevLett.96.104502.

[34] G.R. Moss, J.P. Rothstein, Flow of wormlike micelle solutions through a periodic array of cylinders, J. Non-Newton. Fluid Mech. 165 (1–2) (2010) 1–13, http://dx.doi.org/10.1016/j.jnnfm.2009.08.007.

[35] G.R. Moss, J.P. Rothstein, Flow of wormlike micelle solutions past a confined circular cylinder, J. Non-Newton. Fluid Mech. 165 (21–22) (2010) 1505–1515, http://dx.doi.org/10.1016/j.jnnfm.2010.07.014.

[36] Y. Zhao, A.Q. Shen, S.J. Haward, Flow of wormlike micellar solutions around confined microfluidic cylinders, Soft Matter 12 (42) (2016) 8666–8681, http://dx.doi.org/10.1039/C6SM01597B.

[37] S.J. Haward, N. Kitajima, K. Toda-Peters, T. Takahashi, A.Q. Shen, Flow of wormlike micellar solutions around microfluidic cylinders with high aspect ratio and low blockage ratio, Soft Matter 15 (9) (2019) 1927–1941, http://dx.doi.org/10.1039/C8SM02099J.

[38] C.C. Hopkins, S.J. Haward, A.Q. Shen, Tristability in viscoelastic flow past side-by-side microcylinders, Phys. Rev. Lett. 126 (5) (2021) 054501, http://dx.doi.org/10.1103/PhysRevLett.126.054501.

[39] S.J. Haward, C.C. Hopkins, A.Q. Shen, Stagnation points control chaotic fluctuations in viscoelastic porous media flow, Proc. Natl. Acad. Sci. 118 (38) (2021) e2111651118, http://dx.doi.org/10.1073/pnas.2111651118.

[40] A.A. Dey, Y. Modarres-Sadeghi, J.P. Rothstein, Experimental observation of viscoelastic fluid–structure interactions, J. Fluid Mech. 813 (2017) http://dx.doi.org/10.1017/jfm.2017.15.

[41] C.C. Hopkins, S.J. Haward, A.Q. Shen, Purely elastic fluid–structure interactions in microfluidics: implications for mucociliary flows, Small 16 (9) (2020) 1903872, http://dx.doi.org/10.1002/smll.201903872.

[42] A.A. Dey, Y. Modarres-Sadeghi, J.P. Rothstein, Viscoelastic flow-induced oscillations of a cantilevered beam in the crossflow of a wormlike micelle solution, J. Non-Newton. Fluid Mech. 286 (2020) 104433, http://dx.doi.org/10.1016/j.jnnfm.2020.104433.

[43] M.E. Cates, Nonlinear viscoelasticity of wormlike micelles (and other reversibly breakable polymers), J. Phys. Chem. 94 (1) (1990) 371–375, http://dx.doi.org/10.1021/j100364a063.

[44] N.A. Spenley, M.E. Cates, T.C.B. McLeish, Nonlinear rheology of wormlike micelles, Phys. Rev. Lett. 71 (6) (1993) 939, http://dx.doi.org/10.1103/PhysRevLett.71.939.

[45] W. Zou, R.G. Larson, A mesoscopic simulation method for predicting the rheology of semi-dilute wormlike micellar solutions, J. Rheol. 58 (3) (2014) 681–721, http://dx.doi.org/10.1122/1.4868875.

[46] A.A. Adams, M.J. Solomon, R.G. Larson, A nonlinear kinetic-rheology model for reversible scission and deformation of unentangled wormlike micelles, J. Rheol. 62 (6) (2018) 1419–1427, http://dx.doi.org/10.1122/1.5041265.

[47] S. Dutta, M.D. Graham, Mechanistic constitutive model for wormlike micelle solutions with flow-induced structure formation, J. Non-Newton. Fluid Mech. 251 (2018) 97–106, http://dx.doi.org/10.1016/j.jnnfm.2017.12.001.

[48] J.D. Peterson, M. Cates, A full-chain tube-based constitutive model for living linear polymers, J. Rheol. 64 (6) (2020) 1465–1496.

[49] J. Peterson, M. Cates, Constitutive models for well-entangled living polymers beyond the fast-breaking limit, J. Rheol. 65 (4) (2021) 633–662.

[50] R.B. Bird, R.C. Armstrong, O. Hassager, Dynamics of Polymeric Liquids. Vol. 1: Fluid Mechanics, Wiley, 1987.

[51] M.W. Johnson Jr., D. Segalman, A model for viscoelastic fluid behavior which allows non-affine deformation, J. Non-Newton. Fluid Mech. 2 (3) (1977) 255–270, http://dx.doi.org/10.1016/0377-0257(77)80003-7.

[52] H. Giesekus, A simple constitutive equation for polymer fluids based on the concept of deformation-dependent tensorial mobility, J. Non-Newton. Fluid Mech. 11 (1–2) (1982) 69–109, http://dx.doi.org/10.1016/0377-0257(82)85016-7.

[53] J.D. Peterson, L. Gary Leal, Predictions for flow-induced scission in well-entangled living polymers: The living rolie-poly model, J. Rheol. 65 (5) (2021) 959–982.

[54] A. Kalb, L.A. Villasmil-Urdaneta, M. Cromer, Elastic instability and secondary flow in cross-slot flow of wormlike micellar solutions, J. Non-Newton. Fluid Mech. 262 (2018) 79–91, http://dx.doi.org/10.1016/j.jnnfm.2018.03.012.

[55] M.B. Khan, C. Sasmal, Effect of chain scission on flow characteristics of wormlike micellar solutions past a confined microfluidic cylinder: A numerical analysis, Soft Matter 16 (22) (2020) 5261–5272, http://dx.doi.org/10.1039/D0SM00407C.

[56] M.B. Khan, C. Sasmal, Elastic instabilities and bifurcations in flows of wormlike micellar solutions past single and two vertically aligned microcylinders: Effect of blockage and gap ratios, Phys. Fluids 33 (3) (2021) 033109, http://dx.doi.org/10.1063/5.0044318.

[57] F.S. Forte Neto, A.G.B. da Cruz, Stress-gradient-induced migration effects on the elastic instabilities of wormlike micellar solutions in a cross-slot flow, Phys. Fluids 33 (4) (2021) 043108, http://dx.doi.org/10.1063/5.0046759.

[58] M. Cromer, L.P. Cook, G.H. McKinley, Extensional flow of wormlike micellar solutions, Chem. Eng. Sci. 64 (22) (2009) 4588–4596.

[59] E.J. Hemingway, H. Kusumaatmaja, S.M. Fielding, Edge fracture in complex fluids, Phys. Rev. Lett. 119 (2) (2017) 028006.

[60] E.J. Hemingway, S.M. Fielding, Interplay of edge fracture and shear banding in complex fluids, J. Rheol. 64 (5) (2020) 1147–1159.

[61] N. Germann, A. Kate Gurnon, L. Zhou, L. Pamela Cook, A.N. Beris, N.J. Wagner, Validation of constitutive modeling of shear banding, threadlike wormlike micellar fluids, J. Rheol. 60 (5) (2016) 983–999, http://dx.doi.org/10.1122/1.4959292.

[62] N. Germann, L.P. Cook, A.N. Beris, Investigation of the inhomogeneous shear flow of a wormlike micellar solution using a thermodynamically consistent model, J. Non-Newton. Fluid Mech. 207 (2014) 21–31, http://dx.doi.org/10.1016/j.jnnfm.2014.02.005.

[63] C.J. Pipe, N.J. Kim, P.A. Vasquez, L.P. Cook, G.H. McKinley, Wormlike micellar solutions: II. Comparison between experimental data and scission model predictions, J. Rheol. 54 (4) (2010) 881–913, http://dx.doi.org/10.1122/1.3439729.

[64] L. Zhou, P.A. Vasquez, L.P. Cook, G.H. McKinley, Modeling the inhomogeneous response and formation of shear bands in steady and transient flows of entangled liquids, J. Rheol. 52 (2) (2008) 591–623, http://dx.doi.org/10.1122/1.2829769.

[65] S. Varchanis, G. Makrigiorgos, P. Moschopoulos, Y. Dimakopoulos, J. Tsamopoulos, Modeling the rheology of thixotropic elasto-visco-plastic materials, J. Rheol. 63 (4) (2019) 609–639, http://dx.doi.org/10.1122/1.5049136.

[66] A.S. Lodge, Body Tensor Fields in Continuum Mechanics: With Applications to Polymer Rheology, Academic Press, 2014.

[67] A.W. El-Kareh, L.G. Leal, Existence of solutions for all Deborah numbers for a non-Newtonian model modified to include diffusion, J. Non-Newton. Fluid Mech. 33 (3) (1989) 257–287, http://dx.doi.org/10.1016/0377-0257(89)80002-3.

[68] C.-Y.D. Lu, P.D. Olmsted, R.C. Ball, Effects of nonlocal stress on the determination of shear banding flow, Phys. Rev. Lett. 84 (4) (2000) 642, http://dx.doi.org/10.1103/PhysRevLett.84.642.

[69] S. Varchanis, Y. Dimakopoulos, J. Tsamopoulos, Evaluation of tube models for linear entangled polymers in simple and complex flows, J. Rheol. 62 (1) (2018) 25–47, http://dx.doi.org/10.1122/1.5009197.

[70] S. Varchanis, Y. Dimakopoulos, C. Wagner, J. Tsamopoulos, How viscoelastic is human blood plasma? Soft Matter 14 (21) (2018) 4238–4251, http://dx.doi.org/10.1039/C8SM00061A.

[71] S. Varchanis, A. Kordalis, Y. Dimakopoulos, J. Tsamopoulos, Adhesion, cavitation, and fibrillation during the debonding process of pressure sensitive adhesives, Phys. Rev. Fluids 6 (1) (2021) 013301, http://dx.doi.org/10.1103/PhysRevFluids.6.013301.

[72] V. Calabrese, S. Varchanis, S.J. Haward, J. Tsamopoulos, A.Q. Shen, Structure-property relationship of a soft colloidal glass in simple and mixed flows, J. Colloid Interface Sci. 601 (2021) 454–466, http://dx.doi.org/10.1016/j.jcis.2021.05.103.

[73] F. Bautista, J.M. De Santos, J.E. Puig, O. Manero, Understanding thixotropic and antithixotropic behavior of viscoelastic micellar solutions and liquid crystalline dispersions. I. The model, J. Non-Newton. Fluid Mech. 80 (2–3) (1999) 93–113, http://dx.doi.org/10.1016/S0377-0257(98)00081-0.

[74] F. Bautista, J.F.A. Soltero, J.H. Pérez-López, J.E. Puig, O. Manero, On the shear banding flow of elongated micellar solutions, J. Non-Newton. Fluid Mech. 94 (1) (2000) 57–66, http://dx.doi.org/10.1016/S0377-0257(00)00128-2.

[75] O. Manero, F. Bautista, J.F.A. Soltero, J.E. Puig, Dynamics of worm-like micelles: the Cox-Merz rule, J. Non-Newton. Fluid Mech. 106 (1) (2002) 1–15, http://dx.doi.org/10.1016/S0377-0257(02)00082-4.

[76] S. Tabatabaei, J.E. López-Aguilar, H.R. Tamaddon-Jahromi, M.F. Webster, R. Williams, Modified Bautista–Manero (MBM) modelling for hyperbolic contraction-expansion flows, Rheol. Acta 54 (11) (2015) 869–885, http://dx.doi.org/10.1007/s00397-015-0870-y.

[77] J.E. López-Aguilar, M.F. Webster, H.R. Tamaddon-Jahromi, O. Manero, Convoluted models and high-Weissenberg predictions for micellar thixotropic fluids in contraction-expansion flows, J. Non-Newton. Fluid Mech. 232 (2016) 55–66, http://dx.doi.org/10.1016/j.jnnfm.2016.03.004.

[78] A.G. Fredrickson, A model for the thixotropy of suspensions, AIChE J. 16 (3) (1970) 436–441, http://dx.doi.org/10.1002/aic.690160321.

[79] M. Grmela, F. Chinesta, A. Ammar, Mesoscopic tube model of fluids composed of worm-like micelles, Rheol. Acta 49 (5) (2010) 495–506, http://dx.doi.org/10.1007/s00397-009-0428-y.
[80] N. Germann, L.P. Cook, A.N. Beris, Nonequilibrium thermodynamic modeling of the structure and rheology of concentrated wormlike micellar solutions, J. Non-Newton. Fluid Mech. 196 (2013) 51–57, http://dx.doi.org/10.1016/j.jnnfm.2012.12.010.
[81] H. Rehage, H. Hoffmann, Rheological properties of viscoelastic surfactant systems, J. Phys. Chem. 92 (16) (1988) 4712–4719, http://dx.doi.org/10.1021/j100327a031.
[82] S.M. Fielding, Linear instability of planar shear banded flow, Phys. Rev. Lett. 95 (13) (2005) 134501, http://dx.doi.org/10.1103/PhysRevLett.95.134501.
[83] C. Grand, J. Arrault, M. Cates, Slow transients and metastability in wormlike micelle rheology, J. Phys. II 7 (8) (1997) 1071–1086.
[84] S. Lerouge, P.D. Olmsted, Non-local effects in shear banding of polymeric flows, Front. Phys. 7 (2020) 246, http://dx.doi.org/10.3389/fphy.2019.00246.
[85] H. Mohammadigoushki, S.J. Muller, A flow visualization and superposition rheology study of shear-banding wormlike micelle solutions, Soft Matter 12 (4) (2016) 1051–1061, http://dx.doi.org/10.1039/C5SM02266E.
[86] C. Masselon, J.-B. Salmon, A. Colin, Nonlocal effects in flows of wormlike micellar solutions, Phys. Rev. Lett. 100 (3) (2008) 038301, http://dx.doi.org/10.1103/PhysRevLett.100.038301.
[87] M.-A. Fardin, O. Radulescu, A. Morozov, O. Cardoso, J. Browaeys, S. Lerouge, Stress diffusion in shear banding wormlike micelles, J. Rheol. 59 (6) (2015) 1335–1362, http://dx.doi.org/10.1122/1.4930858.
[88] P.D. Olmsted, O. Radulescu, C.-Y.D. Lu, Johnson–Segalman model with a diffusion term in cylindrical Couette flow, J. Rheol. 44 (2) (2000) 257–275, http://dx.doi.org/10.1122/1.551085.
[89] S.M. Fielding, P.D. Olmsted, Flow phase diagrams for concentration-coupled shear banding, Eur. Phys. J. E 11 (1) (2003) 65–83, http://dx.doi.org/10.1140/epje/i2002-10128-7.
[90] R.L. Moorcroft, S.M. Fielding, Shear banding in time-dependent flows of polymers and wormlike micelles, J. Rheol. 58 (1) (2014) 103–147, http://dx.doi.org/10.1122/1.4842155.
[91] T.C. Papanastasiou, N. Malamataris, K. Ellwood, A new outflow boundary condition, Internat. J. Numer. Methods Fluids 14 (5) (1992) 587–608, http://dx.doi.org/10.1002/fld.1650140506.
[92] J.M. Adams, S.M. Fielding, P.D. Olmsted, The interplay between boundary conditions and flow geometries in shear banding: Hysteresis, band configurations, and surface transitions, J. Non-Newton. Fluid Mech. 151 (1–3) (2008) 101–118, http://dx.doi.org/10.1016/j.jnnfm.2008.01.008.
[93] S. Varchanis, A. Syrakos, Y. Dimakopoulos, J. Tsamopoulos, A new finite element formulation for viscoelastic flows: Circumventing simultaneously the LBB condition and the high-Weissenberg number problem, J. Non-Newton. Fluid Mech. 267 (2019) 78–97, http://dx.doi.org/10.1016/j.jnnfm.2019.04.003.
[94] S. Varchanis, A. Syrakos, Y. Dimakopoulos, J. Tsamopoulos, PEGAFEM-V: A new Petrov-Galerkin finite element method for free surface viscoelastic flows, J. Non-Newton. Fluid Mech. 284 (2020) 104365, http://dx.doi.org/10.1016/j.jnnfm.2020.104365.
[95] S. Varchanis, J. Tsamopoulos, Numerical simulations of interfacial and elastic instabilities, 2021, URL http://pcwww.liv.ac.uk/robpoole/jnnfm/vids/Patras_JNNFM_28042021.mp4.
[96] E.J. Doedel, V.A. Romanov, R.C. Paffenroth, H.B. Keller, D.J. Dichmann, J. Galán-Vioque, A. Vanderbauwhede, Elemental periodic orbits associated with the libration points in the circular restricted 3-body problem, Int. J. Bifurcation Chaos 17 (08) (2007) 2625–2677, http://dx.doi.org/10.1142/S0218127407018671.
[97] S. Varchanis, Y. Dimakopoulos, J. Tsamopoulos, Steady film flow over a substrate with rectangular trenches forming air inclusions, Phys. Rev. Fluids 2 (12) (2017) 124001, http://dx.doi.org/10.1103/PhysRevFluids.2.124001.
[98] P.E. Arratia, C.C. Thomas, J. Diorio, J.P. Gollub, Elastic instabilities of polymer solutions in cross-channel flow, Phys. Rev. Lett. 96 (14) (2006) 144502, http://dx.doi.org/10.1103/PhysRevLett.96.144502.
[99] R.J. Poole, M.A. Alves, P.J. Oliveira, Purely elastic flow asymmetries, Phys. Rev. Lett. 99 (16) (2007) 164503, http://dx.doi.org/10.1103/PhysRevLett.99.164503.
[100] T.J. Ober, J. Soulages, G.H. McKinley, Spatially resolved quantitative rheo-optics of complex fluids in a microfluidic device, J. Rheol. 55 (5) (2011) 1127–1159, http://dx.doi.org/10.1122/1.3606593.
[101] G.G. Fuller, Optical Rheometry of Complex Fluids, Oxford University Press on Demand, 1995.
[102] G.N. Rocha, R.J. Poole, M.A. Alves, P.J. Oliveira, On extensibility effects in the cross-slot flow bifurcation, J. Non-Newton. Fluid Mech. 156 (1–2) (2009) 58–69, http://dx.doi.org/10.1016/j.jnnfm.2008.06.008.
[103] S.J. Haward, G.H. McKinley, A.Q. Shen, Elastic instabilities in planar elongational flow of monodisperse polymer solutions, Sci. Rep. 6 (1) (2016) 33029, http://dx.doi.org/10.1038/srep33029.
[104] S.J. Haward, M.S.N. Oliveira, M.A. Alves, G.H. McKinley, Optimized cross-slot flow geometry for microfluidic extensional rheometry, Phys. Rev. Lett. 109 (12) (2012) 128301, http://dx.doi.org/10.1103/PhysRevLett.109.128301.
[105] A. Lanzaro, D. Corbett, X.-F. Yuan, Non-linear dynamics of semi-dilute PAAM solutions in a microfluidic 3D cross-slot flow geometry, J. Non-Newton. Fluid Mech. 242 (2017) 57–65, http://dx.doi.org/10.1016/j.jnnfm.2017.02.006.
[106] A. Kordalis, S. Varchanis, G. Ioannou, Y. Dimakopoulos, J. Tsamopoulos, Investigation of the extensional properties of elasto-visco-plastic materials in cross-slot geometries, J. Non-Newton. Fluid Mech. 296 (2021) 104627, http://dx.doi.org/10.1016/j.jnnfm.2021.104627.
[107] S. Varchanis, D. Pettas, Y. Dimakopoulos, J. Tsamopoulos, Origin of the Sharkskin instability: Nonlinear dynamics, Phys. Rev. Lett. 127 (8) (2021) 088001, http://dx.doi.org/10.1103/PhysRevLett.127.088001.
[108] S.J. Haward, C.C. Hopkins, A.Q. Shen, Asymmetric flow of polymer solutions around microfluidic cylinders: Interaction between shear-thinning and viscoelasticity, J. Non-Newton. Fluid Mech. 278 (2020) 104250, http://dx.doi.org/10.1016/j.jnnfm.2020.104250.
[109] S. Varchanis, C.C. Hopkins, A.Q. Shen, J. Tsamopoulos, S.J. Haward, Asymmetric flows of complex fluids past confined cylinders: A comprehensive numerical study with experimental validation, Phys. Fluids 32 (5) (2020) 053103, http://dx.doi.org/10.1063/5.0008783.
[110] S.J. Haward, C.C. Hopkins, S. Varchanis, A.Q. Shen, Bifurcations in flows of complex fluids around microfluidic cylinders, Lab Chip (2021) http://dx.doi.org/10.1039/D1LC00128K.